ALMA INVESTIGATION OF VIBRATIONALLY EXCITED HCN/HCO+/HNC EMISSION LINES IN THE AGN-HOSTING ULTRALUMINOUS INFRARED GALAXY IRAS 20551−4250

Masatoshi Imanishi (今西昌俊)[1,2,4], Kouichiro Nakanishi (中西康一郎)[2,4], and Takuma Izumi (泉拓磨)[3]

[1] Subaru Telescope, 650 North A'ohoku Place, Hilo, HI 96720, USA; masa.imanishi@nao.ac.jp
[2] National Astronomical Observatory of Japan, 2-21-1 Osawa, Mitaka, Tokyo 181-8588, Japan
[3] Institute of Astronomy, School of Science, The University of Tokyo, 2-21-1 Osawa, Mitaka, Tokyo 181-0015, Japan

ABSTRACT

We present the results of ALMA Cycle 2 observations of the ultraluminous infrared galaxy IRAS 20551−4250 at HCN/HCO+/HNC $J = 3$–2 lines at both vibrational ground ($v = 0$) and vibrationally excited ($v_2 = 1$) levels. This galaxy contains a luminous buried active galactic nucleus (AGN), in addition to starburst activity, and our ALMA Cycle 0 data revealed a tentatively detected vibrationally excited HCN $v_2 = 1f$ $J = 4$–3 emission line. In our ALMA Cycle 2 data, the HCN/HCO+/HNC $J = 3$–2 emission lines at $v = 0$ are clearly detected. The HCN and HNC $v_2 = 1f$ $J = 3$–2 emission lines are also detected, but the HCO+ $v_2 = 1f$ $J = 3$–2 emission line is not. Given the high energy level of $v_2 = 1$ and the resulting difficulty of collisional excitation, we compared these results with those of the calculation of infrared radiative pumping, using the available infrared 5–35 μm spectrum. We found that all of the observational results were reproduced if the HCN abundance was significantly higher than that of HCO+ and HNC. The flux ratio and excitation temperature between $v_2 = 1f$ and $v = 0$, after correction for possible line opacity, suggests that infrared radiative pumping affects rotational (J-level) excitation at $v = 0$ at least for HCN and HNC. The HCN-to-HCO+ $v = 0$ flux ratio is higher than those of starburst-dominated regions, and will increase even more when the derived high HCN opacity is corrected. The enhanced HCN-to-HCO+ flux ratio in this AGN-hosting galaxy can be explained by the high HCN-to-HCO+ abundance ratio and sufficient HCN excitation at up to $J = 4$, rather than the significantly higher efficiency of infrared radiative pumping for HCN than HCO+.

Key words: galaxies: active – galaxies: nuclei – galaxies: Seyfert – galaxies: starburst – quasars: general – submillimeter: galaxies

1. INTRODUCTION

The apparent ubiquity of supermassive blackholes (SMBHs) in the spheroidal components of present day galaxies, and the correlation between the mass of SMBHs and spheroidal stellar components (Magorrian et al. 1998; Ferrarese & Merritt 2000; Gultekin et al. 2009; McConnell & Ma 2013) indicate that the active galactic nucleus (AGN; SMBH-driven activity) and starbursts (active star formation; plausibly the progenitors of spheroids) are physically connected and have co-evolved. Observational constraints on how and when SMBHs grow in mass, in relation to starbursts, is vital for fully understanding the galaxy formation process in the universe.

The widely accepted cold-dark-matter-based galaxy formation scenarios postulate that mergers of gas-rich galaxies with SMBHs at their centers are common throughout the history of the universe (Hopkins et al. 2008). Numerical simulations of such gas-rich galaxy mergers not only suggest that many stars form rapidly in dust-/gas-obscured regions, but also suggest that SMBHs have high-mass accretion rates and become luminous AGNs, deeply buried in the nuclear dust/gas, making such gas-rich galaxy mergers luminous in the infrared (Hopkins et al. 2006). It is essential to evaluate the importance of *buried* AGNs in dust-/gas-rich infrared luminous galaxy mergers by separating them from the surrounding starbursts if we are to observationally understand the physical processes that occur during this key epoch in the co-evolution of stars and SMBHs (Hopkins et al. 2005; Debuhr et al. 2011). However, unlike

optically selected AGNs, where a central mass-accreting SMBH is surrounded by toroidally shaped dust/gas (the so-called dusty molecular torus) and the AGN's radiation can photo-ionize gas clouds along the torus axis above a torus scale height (Antonucci & Millar 1985), deeply buried AGNs are optically elusive and their detection requires observations at wavelengths of low dust extinction.

A buried AGN (mass accretion onto a SMBH) has two different properties from a starburst (nuclear fusion inside stars). First, the efficiency of the AGN's radiative energy generation (6%–42% of Mc^2, where M is the mass of the accreting material and c is the speed of light; Bardeen 1970; Thorne 1974) is much higher than that of nuclear fusion inside stars (~0.7% of Mc^2), so that an AGN has very high surface brightness emission and can heat a large amount of surrounding dust to high temperatures (>100 K), producing a strong mid-infrared 3–20 μm continuum emission. Second, the X-ray to UV luminosity ratio is much higher in an AGN than a starburst (Ranalli et al. 2003; Shang et al. 2011). These differences between an AGN and a starburst could create different effects/feedback to the surrounding material. If we discover AGN-sensitive (sub)millimeter molecular lines, we can disentangle the AGN from the starburst using the flux ratios of these lines, in a manner similar to the optical AGN-starburst spectroscopic classification method, based on the optical emission line flux ratios, which is extensively applied to less dusty galaxies (Veilleux & Osterbrock 1987; Kewley et al. 2001; Kauffmann et al. 2003). Once established, this (sub)millimeter molecular line energy diagnostic method will create a large potential to scrutinize deeply buried AGNs in dust-/gas-rich galaxies out to

---

[4] Department of Astronomical Science, The Graduate University for Advanced Studies (SOKENDAI), Mitaka, Tokyo 181-8588, Japan.

the distant universe, because of (a) very small dust extinction in the (sub)millimeter wavelength range, and (b) the availability of highly sensitive ALMA observing facility.

Based on pre-ALMA (sub)millimeter interferometric $1''$–$5''$ resolution observations of the nuclear regions of nearby bright starburst and Seyfert galaxies (modest luminosity AGNs), the enhanced emission of the dense gas tracer, HCN, at $J = 1$–0 (rotational transition), relative to HCO^+ has been found in AGNs and been proposed as a possible AGN indicator (Kohno 2005; Krips et al. 2008). This was mainly thanks to the spatially resolved investigation of AGN-affected molecular gas by reducing the contamination from spatially extended star-formation-affected molecular gas emission in Seyfert host galaxies, because the contamination could hamper the detection of the signatures of AGN-affected molecular gas emission in large-aperture, single-dish telescope observations (Gracia-Carpio et al. 2006; Baan et al. 2008; Costagliola et al. 2011; Snell et al. 2011). Subsequent interferometric observations have also confirmed enhanced HCN $J = 1$–0 emission in the nuclei of dust-/gas-rich merging luminous infrared galaxies (LIRGs; infrared (8–1000 μm luminosity $L_{IR} > 10^{11}L_{\odot}$), which are diagnosed as buried-AGN-important based on infrared spectroscopy, compared to starburst-dominated LIRGs (Imanishi et al. 2004, 2006, 2007b, 2009; Imanishi & Nakanishi 2006). Based on recent single-dish telescope observations, a similar trend of HCN $J = 1$–0 flux excess, relative to HCO^+ $J = 1$–0, has been confirmed for infrared-classified, AGN-important LIRGs compared to starburst-dominated LIRGs (Privon et al. 2015). ALMA Cycle 0–1 interferometric observations further support HCN emission enhancement relative to HCO^+ in the nuclei of AGN-important LIRGs compared to starburst regions at $J = 4$–3 (Imanishi & Nakanishi 2013a, 2013b, 2014; Iono et al. 2013; Garcia-Burillo et al. 2014; Izumi et al. 2015). It has now become clear that luminous AGNs tend to show enhanced HCN emission. However, the physical interpretation of enhanced HCN emission in AGNs is still unclear. Although HCN abundance enhancement in an AGN is proposed in some chemical calculations, because of high gas/dust temperature and/or X-ray irradiation (Meijerink & Spaans 2005; Lintott & Viti 2006; Harada et al. 2010), it is also calculated that the HCN-to-HCO^+ abundance ratio in molecular gas around an AGN can vary dramatically depending on assumed physical parameters (Meijerink & Spaans 2005; Harada et al. 2013). Additionally, even if HCN abundance is indeed enhanced in an AGN, the widely assumed collisional excitation alone does not seem to be enough to reproduce the strong HCN rotational J-transition emission lines observed in some AGNs (Yamada et al. 2007).

An infrared radiative pumping mechanism has been proposed to be a plausible scenario for the enhancement of HCN rotational J-transition emission in AGNs (Aalto et al. 1995; Garcia-Burillo et al. 2006; Weiss et al. 2007). Specifically, HCN can be vibrationally excited to $v_2 = 1$ by absorbing infrared 14 μm photons (Townes & Schawlow 1975). Through the decay back to the vibrational-ground level ($v = 0$), the HCN rotational J-transition flux at $v = 0$ can be stronger than collisional excitation alone (Rangwala et al. 2011). Since an AGN can emit infrared 14 μm continuum emission much more strongly than a starburst due to AGN-heated hot (>100 K) dust, such an infrared radiative pumping mechanism for HCN should work more effectively in an AGN than in a starburst. In fact, the HCN $v_2 = 1$–0 *absorption*

features were seen at infrared 14 μm in several obscured AGNs (Lahuis et al. 2007), and the vibrationally excited HCN $v_2 = 1$, l=1f (hereafter $v_2 = 1$f), $J = 4$–3, and/or $J = 3$–2 *emission* lines in the (sub)millimeter wavelength have recently been detected in several AGN-hosting LIRGs (Sakamoto et al. 2010; Imanishi & Nakanishi 2013b; Aalto et al. 2015a, 2015b; Costagliola et al. 2015), supporting the scenario that infrared radiative pumping actually works in some AGNs to vibrationally excite HCN and could contribute to an increase in HCN J-transition flux at $v = 0$.

However, the other dense gas tracers, HCO^+ and HNC, also have absorption features at infrared ~12 μm and ~21.5 μm, respectively (Davies et al. 1984; Kawaguchi et al. 1985; Burkholder et al. 1987), and could therefore be vibrationally excited to $v_2 = 1$ by infrared radiative pumping. If the infrared radiative pumping mechanism is responsible for the enhanced HCN J-transition emission at $v = 0$ in AGNs, its efficiency must be particularly high for HCN only. A comparison of the strengths of the $v_2 = 1$ emission lines for HCN, HCO^+, and HNC is the most straightforward way to test the scenario of whether infrared radiative pumping works most efficiently for HCN and selectively boosts HCN J-transition flux at $v = 0$. No meaningful observational constraints are placed in external galaxies for the strengths of HCO^+ and HNC $v_2 = 1$f J-transition lines, except for the report concerning the detection of HNC $v_2 = 1$f $J = 3$–2 emission line in the AGN-hosting LIRG NGC 4418 (Costagliola et al. 2013).

We conducted ALMA Cycle 2 observations of the LIRG IRAS 20551−4250 ($z = 0.043$) to investigate the relative strength of vibrationally excited ($v_2 = 1$) HCN, HCO^+, and HNC J-transition lines. IRAS 20551−4250 is categorized as an ultraluminous infrared galaxy (ULIRG) with an infrared (8–1000 μm) luminosity $L_{IR} = 10^{12.0}L_{\odot}$, and has far-infrared (40–500 μm) luminosity $L_{FIR} = 10^{11.9}L_{\odot}$ (see Table 1 of Imanishi & Nakanishi 2013b). It consists of a main single nucleus with a signature of long merging tail in the southern direction (Duc et al. 1997; Rothberg & Joseph 2004). It is classified optically as a LINER/H II-region; namely, it has no obvious optical AGN (Seyfert) signature (Duc et al. 1997; Yuan et al. 2010). Based on several energy diagnostic methods using infrared and X-ray spectroscopy, the signature of a luminous, energetically significant (20%–60% of the bolometric luminosity) buried AGN was identified in IRAS 20551−4250 in addition to starburst activity (Franceschini et al. 2003; Risaliti et al. 2006; Nardini et al. 2008, 2009, 2010; Sani et al. 2008; Imanishi et al. 2010b, 2011; Veilleux et al. 2013). The vibrationally excited HCN $v_2 = 1$f $J = 4$–3 emission line was tentatively detected with our ALMA Cycle 0 data because of small molecular line widths, which enable us to clearly separate the HCN $v_2 = 1$f $J = 4$–3 emission line from the nearby, much brighter HCO^+ $v = 0$ $J = 4$–3 emission line (Imanishi & Nakanishi 2013b). Thus, IRAS 20551−4250 is a very good target for investigating the relative strength of vibrationally excited $HCN/HCO^+/HNC$ J-transition emission lines, and how the infrared radiative pumping mechanism affects the rotational excitation of $HCN/HCO^+/HNC$ at $v = 0$.

In the present paper, we report the results of ALMA Cycle 2 observations of the AGN-hosting ULIRG IRAS 20551−4250 at HCN, HCO^+, and HNC lines at both the vibrational ground ($v = 0$) and vibrationally excited ($v_2 = 1$) levels. Throughout this paper, we adopt $H_0 = 71$ km s^{-1} Mpc^{-1}, $\Omega_M = 0.27$, and $\Omega_\Lambda = 0.73$ (Komatsu et al. 2009), in which case the luminosity

IMANISHI (今西昌俊), NAKANISHI (中西康一郎), & IZUMI (泉拓磨)

Table 1
Log of Our ALMA Cycle 2 Observations

Line	Date	Antenna Number	Baseline (m)	Integration Time (min)	Calibrator		
	(UT)				Bandpass	Flux	Phase
(1)	(2)	(3)	(4)	(5)	(6)	(7)	(8)
HCN/HCO$^+$ $J = 3$–2	2014 May 17	35	15–650	14	J2056−4714	J2056−4714	J2056−4714
HNC $J = 3$–2	2014 May 17	35	15–650	36	J2056−4714	J2056−4714	J2056−4714

Note. Col. (1): Observed line. Col. (2): Observation date (UT). Col. (3): Number of antennas used for observations. Col. (4): Baseline length in meter. Minimum and maximum baseline lengths are shown. Col. (5): Net on-source integration time in minutes. Cols. (6), (7), and (8): Bandpass, flux, and phase calibrator for the target source, respectively. The flux density of J2056−4714 is estimated from ALMA monitoring observations.
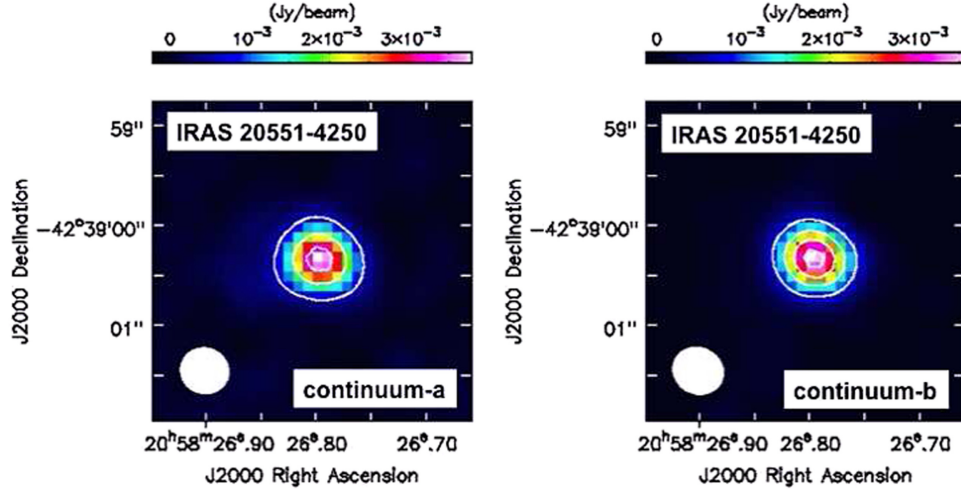

Figure 1. Continuum-a (central observed frequency $\nu_{center} \sim 256.3$ GHz) and continuum-b ($\nu_{center} \sim 254.5$ GHz) data taken during the observations of HCN/HCO$^+$ $J = 3$–2 and HNC $J = 3$–2, respectively. The contours represent the 10σ, 30σ, and 50σ levels for continuum-a and 20σ, 40σ, 60σ, and 80σ levels for continuum-b.

distance is 188 Mpc and 1 arcsec corresponds to 0.84 kpc at the distance of IRAS 20551−4250. Molecular parameters are derived from the Cologne Database of Molecular Spectroscopy (CDMS; Müller et al. 2005) via Splatalogue (http://www.splatalogue.net). For molecular transitions, where there is no indication of v (the vibrational level), we mean $v = 0$ (i.e., the vibrational ground level). When we write HCN, HCO$^+$, and HNC in this manuscript, we mean H^{12}C^{14}N, H^{12}C^{16}O$^+$, and H^{14}N^{12}C, respectively.

2. OBSERVATIONS AND DATA ANALYSIS

Our ALMA Cycle 2 observations in band 6 (211–275 GHz) were undertaken within the program 2013.1.00033.S (PI = M. Imanishi). The details of our observations are given in Table 1. We adopted the widest 1.875 GHz band mode and 3840 total channel number for our observations. We requested $<0\farcs6$ spatial resolution in our proposal.

We employed three spectral windows in USB in band 6 to cover (a) HCN $J = 3$–2 (rest-frame frequency is $\nu_{rest} = 265.89$ GHz), (b) HCO$^+$ $J = 3$–2 ($\nu_{rest} = 267.56$ GHz) and HCN $v_2 = 1f$ $J = 3$–2 ($\nu_{rest} = 267.20$ GHz), and (c) HCO$^+$ $v_2 = 1f$ $J = 3$–2 ($\nu_{rest} = 268.69$ GHz) in each of the three spectral windows. The HCN and HCO$^+$ $J = 3$–2 emission lines can therefore be obtained at both the vibrational ground ($v = 0$) and vibrationally excited ($v_2 = 1f$) levels concurrently.

We also conducted additional independent observations for HNC $J = 3$–2 ($\nu_{rest} = 271.98$ GHz) and HNC $v_2 = 1f$ $J = 3$–2 ($\nu_{rest} = 273.87$ GHz). We employed four spectral windows, of

which two in USB were used to cover HNC $J = 3$–2 and HNC $v_2 = 1f$ $J = 3$–2 lines. The remaining two spectral windows in LSB were used to probe continuum emission and serendipitously detected emission lines.

We used CASA (Petry et al. 2012) for our data analysis. We first checked the visibility plots in calibrated data provided by the Joint ALMA Observatory and found that the presence of HCN, HCO$^+$, and HNC $J = 3$–2 emission lines was clearly recognizable. Signatures of other weak emission lines were also seen in some spectral windows. We selected channels that were not clearly affected by detected emission line features and estimated the continuum flux levels by using data in (a) three spectral windows for HCN/HCO$^+$ observations, and (b) four spectral windows for HNC observations. After subtracting these estimated continuum levels, we performed the task "clean" for the detected emission line data. We also applied the "clean" procedure for the continuum data. We employed 40 channel spectral binning (~ 20 km s^{-1}), and adopted a pixel scale of $0\farcs1$ pixel^{-1} in this clean procedure. The maximum recoverable scale in our data is $\sim 10''$. In ALMA Cycle 2, the absolute calibration uncertainty is expected to be $<10\%$ in band 6, which will not significantly affect our main discussion.

3. RESULTS

From our observations, two continuum data were obtained. Figure 1 displays continuum-a (taken with the HCN and HCO$^+$ $J = 3$–2 observations) and continuum-b (taken with HNC $J = 3$–2) maps. Table 2 presents the continuum emission properties. The achieved spatial resolution is $\sim 0\farcs5$ (~ 420 pc) (Table 2,

Table 2
Continuum Emission

Frequency (GHz) (1)	Flux (mJy beam^{-1}) (2)	Peak Coordinate (R.A., Decl.)J2000 (3)	rms (mJy beam^{-1}) (4)	Synthesized Beam (arcsec × arcsec) (°) (5)
a: 244.8–246.6, 247.1–249.0, 259.8–263.5	3.8 (59σ)	(20 58 26.80, −42 39 00.3)	0.065	0.50 × 0.46 (74°)
b: 254.0–258.5	3.6 (88σ)	(20 58 26.80, −42 39 00.3)	0.041	0.52 × 0.47 (66°)

Note. Col. (1): Frequency range in (GHz) used for extraction of continuum-a (taken simultaneously with HCN and HCO$^+$ $J = 3$–2 observations), and continuum-b (obtained at the same time as HNC $J = 3$–2 observations). Frequencies at obvious emission line features are removed. Col. (2): Flux in (mJy beam^{-1}) at the emission peak. Value at the highest flux pixel (0$\farcs$1 pixel^{-1}) is extracted. The detection significance relative to the rms noise is shown in parentheses. Possible systematic uncertainty is not included. Col. (3): The coordinate of the continuum emission peak in J2000. Col. (4): The rms noise level (1σ) in (mJy beam^{-1}). Col. (5): Synthesized beam in (arcsec × arcsec) and position angle in (°). The position angle is 0° along the north–south direction and increases in the counterclockwise direction.

column 5) and meets our request of <0$\farcs$6. Using the CASA task "imfit," we estimate the deconvolved, intrinsic emission size to be 0$\farcs$28 × 0$\farcs$23 (240 pc × 190 pc) for continuum-a and 0$\farcs$28 × 0$\farcs$24 (240 pc × 205 pc) for continuum-b, with uncertainties of <20 pc, where the values along the major and minor axes are shown. Continuum emission is estimated to have a spatial extent with about half of the ALMA synthesized beam size. These independently taken continuum data show consistent results in terms of peak position, peak flux, and morphology. To understand the physical origin of the detected continuum emission, we assume that half of the far-infrared (40–500 μm) luminosity of IRAS 20551−4250 comes from starburst activity, because (a) the AGN bolometric contribution in IRAS 20551−4250 is estimated to be 20%–60% (Nardini et al. 2008, 2009, 2010; Veilleux et al. 2013), and (b) the bolometric luminosity of IRAS 20551−4250 is dominated by far-infrared (40–500 μm) emission ($L_{\rm FIR} = 10^{11.9} L_\odot$; Section 1). The contribution from thermal free–free emission in starburst H II regions at ~255 GHz is estimated to be ~1.6 mJy, using Equation (1) of Nakanishi et al. (2005). This is a significant contribution to the observed continuum flux at ~255 GHz with 3.6–3.8 mJy. If the starburst contribution to the observed far-infrared luminosity is higher than 50%, the free–free emission flux at ~255 GHz will be even higher. Therefore, we infer that the detected continuum emission (~3.6–3.8 mJy) at ~255 GHz is a combination of thermal free–free emission from starburst H II regions and dust emission heated by dust-obscured energy sources (AGNs and/or starburst). Since the detected continuum emission is spatially compact with <250 pc (Figure 1), the thermal free–free emission should be of nuclear starburst origin.

A full spectrum taken with our ALMA observations at the continuum peak position within the beam size is shown in Figure 2. In the spectrum taken with HCN/HCO$^+$ $J = 3$–2 lines, the HCN $v_2 = 1$f $J = 3$–2 emission line is visible, but the HCO$^+$ $v_2 = 1$f $J = 3$–2 line is not (Figure 2(c)). In the spectrum taken with the HNC $J = 3$–2 line, the HNC $v_2 = 1$f $J = 3$–2 emission line is detected (Figure 2(e)). We also serendipitously detected several other emission lines. In the spectrum taken with HCN/HCO$^+$ $J = 3$–2 lines, an emission line is recognizable at the observed frequency $\nu_{\rm obs} \sim 257.40$ GHz, or rest-frame frequency $\nu_{\rm rest} \sim 268.47$ GHz. We ascribe this emission line to HOC$^+$ $J = 3$–2 ($v = 0$) at $\nu_{\rm rest} = 268.45$ GHz, which was strongly detected in the Galactic star-forming regions (Apponi & Ziurys 1997; Apponi et al. 1999; Savage & Ziurys 2004) and LIRGs (Aalto et al. 2015b, 2015a).

In the spectrum taken with the HNC $J = 3$–2 line, emission lines are identifiable at $\nu_{\rm obs} \sim 245.75, 247.60, 248.35, 261.65$,

and 262.15 GHz. The third and fourth lines at $\nu_{\rm obs} \sim$ 248.35 GHz and 261.65 GHz correspond to the rest-frame frequencies of $\nu_{\rm rest} \sim 259.0$ GHz and 272.9 GHz, which we ascribe to H^{13}CN $J = 3$–2 ($\nu_{\rm rest} \sim 259.01$ GHz) and HC$_3$N $J = 30$–29 ($\nu_{\rm rest} \sim 272.88$ GHz) (Costagliola & Aalto 2010; Costagliola et al. 2013), respectively. The first and second lines at $\nu_{\rm obs} \sim 245.75$ GHz and 247.60 GHz correspond to $\nu_{\rm rest} \sim 256.3$ GHz and 258.2 GHz, which we tentatively attribute to SO$_2$ 5(3,3)–5(2,4) ($\nu_{\rm rest} \sim 256.25$ GHz) and SO 6(6)–5(5) ($\nu_{\rm rest} \sim 258.26$ GHz), respectively, because these lines are the strongest in these frequency ranges in the Galactic star-forming region Orion A (Blake et al. 1986; Greaves & White 1991). For the second line, the HC^{15}N $J = 3$–2 emission line ($\nu_{\rm rest} \sim 258.16$ GHz) might make some contribution. For the fifth line at $\nu_{\rm obs} \sim 262.15$ GHz, or $\nu_{\rm rest} \sim 273.4$ GHz, we tentatively assign it as CH$_3$CCH 16(2)–15(2) ($\nu_{\rm rest} \sim 273.40$ GHz), based on the extragalactic detection in the Splatalogue database (http://www.splatalogue.net).

We note that the rest frequencies of $v_2 = 1$e $J = 3$–2 for HCN ($\nu_{\rm rest} = 265.85$ GHz), HCO$^+$ ($\nu_{\rm rest} = 267.42$ GHz), and HNC ($\nu_{\rm rest} = 271.92$ GHz) are so close to the $v = 0$ $J = 3$–2 line for each molecule that it is very difficult to separate the $v_2 = 1$e $J = 3$–2 lines from the much stronger $v = 0$ $J = 3$–2 emission lines. The fluxes of the $v_2 = 1$e emission lines of HCN/HCO$^+$/HNC will not be discussed in this paper.

We create integrated intensity (moment 0) maps of individual molecular lines by combining channels with clear signal signs. Figure 3 displays these maps. Table 3 summarizes their properties. The achieved spatial resolution is ~0$\farcs$5 (~420 pc) for all molecular emission lines (Table 3, column 6), and so our request of <0$\farcs$6 is fulfilled. The molecular line peak positions agree with the continuum emission peak within 1 pixel (0$\farcs$1) in the R.A. and decl. directions for all lines, suggesting that several serendipitously detected faint emission lines are real. The estimated deconvolved intrinsic emission sizes for the brightest HCN, HCO$^+$, and HNC $v = 0$ $J = 3$–2 lines, using the CASA task "imfit," are 0$\farcs$22 × 0$\farcs$20 (185 pc × 170 pc), 0$\farcs$27 × 0$\farcs$26 (225 pc × 220 pc), and 0$\farcs$21 × 0$\farcs$17 (175 pc × 145 pc), with uncertainties of <15 pc, respectively. HCO$^+$ $v = 0$ $J = 3$–2 emission may show slightly larger spatial extension than the HCN $v = 0$ $J = 3$–2 and HNC $v = 0$ $J = 3$–2 emission.

Figure 4 shows spectra around individual molecular lines of our interest at the continuum peak position within the beam size. We fit detected molecular emission lines in the spectra with Gaussian profiles. Table 3 summarizes the fitting results. The flux estimates based on the Gaussian fits will be used in our discussion, except for the non-detected HCO$^+$ $v_2 = 1$f
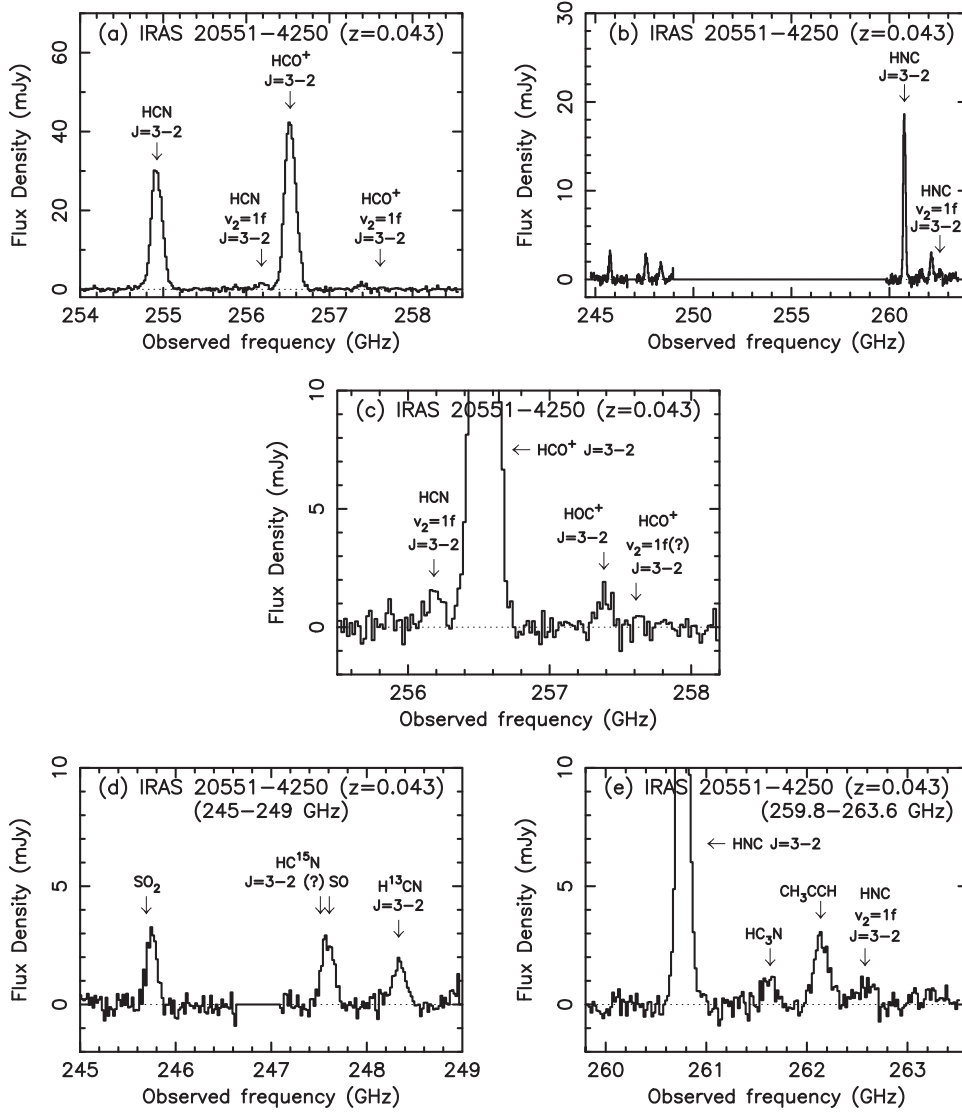
Figure 2. (a) Full spectrum at the continuum peak position within the beam size for the HCN/HCO$^+$ $J = 3$–2 observation. (b) Full spectrum at the continuum peak position within the beam size for the HNC $J = 3$–2 observations. (c) Magnified spectrum around the HCO$^+$ $J = 3$–2 emission line to display the HCN $v_2 = 1f$ $J = 3$–2 and HCO$^+$ $v_2 = 1f$ $J = 3$–2 lines. (d) Magnified spectrum of the lower frequency part for HNC $J = 3$–2 observations to show the serendipitously detected emission lines in more detail. (e) Magnified spectrum of the higher frequency part for the HNC $J = 3$–2 observations to show the serendipitously detected emission lines in more detail. The abscissa is the observed frequency in (GHz) and the ordinate is flux density in (mJy). Down arrows are shown at the expected observed frequency for $z = 0.0430$ for individual molecular emission lines of our interest.

$J = 3$–2 emission line for which the upper limit in the integrated intensity (moment 0) map is adopted. The molecular line luminosities are summarized in Table 4.

Intensity-weighted mean velocity (moment 1) and intensity-weighted velocity dispersion (moment 2) maps for the HCN, HCO$^+$, and HNC $J = 3$–2 ($v = 0$) emission lines are shown in Figure 5. In all moment 1 maps, the northeastern region is redshifted and the southwestern region is blueshifted with respect to the nucleus, suggesting a rotating gas motion. A similar gas motion was seen in the HCN and HCO$^+$ $J = 4$–3 ($v = 0$) emission lines (Imanishi & Nakanishi 2013b), suggesting that the spatial origin of these detected molecular emission lines is similar. A similar rotational gas motion is also seen in the CO $J = 1$–0 emission (Ueda et al. 2014), although the detected CO $J = 1$–0 emission is distributed in a wider area than HCN, HCO$^+$, and HNC, due to its lower critical density and higher brightness.

4. DISCUSSION

4.1. Molecular Line Flux Ratio

In Figure 6, the observed HCN-to-HCO$^+$ $J = 3$–2 and HCN-to-HNC $J = 3$–2 flux ratios of IRAS 20551−4250 are added to the plot for $J = 4$–3 (Imanishi & Nakanishi 2014). The AGN-hosting ULIRG IRAS 20551−4250 shows similar HCN-to-HCO$^+$ flux ratios both at $J = 4$–3 and $J = 3$–2, and the ratios are higher than starburst-dominated regions.

Both the HCN-to-HCO$^+$ and HCN-to-HNC flux ratios can change, depending on (a) abundance ratio resulting from various chemical reactions, (b) the excitation condition, and (c) flux attenuation by line opacity. The flux comparison between $J = 4$–3 (Imanishi & Nakanishi 2013b) and $J = 3$–2 (Table 5) for HCN, HCO$^+$, and HNC shows that the ratios of $J = 4$–3 to $J = 3$–2 flux in (Jy km s^{-1}) are 1.6 ± 0.2 for HCN, 1.7 ± 0.2 for HCO$^+$, and 1.8 ± 0.2 for HNC, where a maximum $\sim$10% absolute calibration uncertainty in individual ALMA
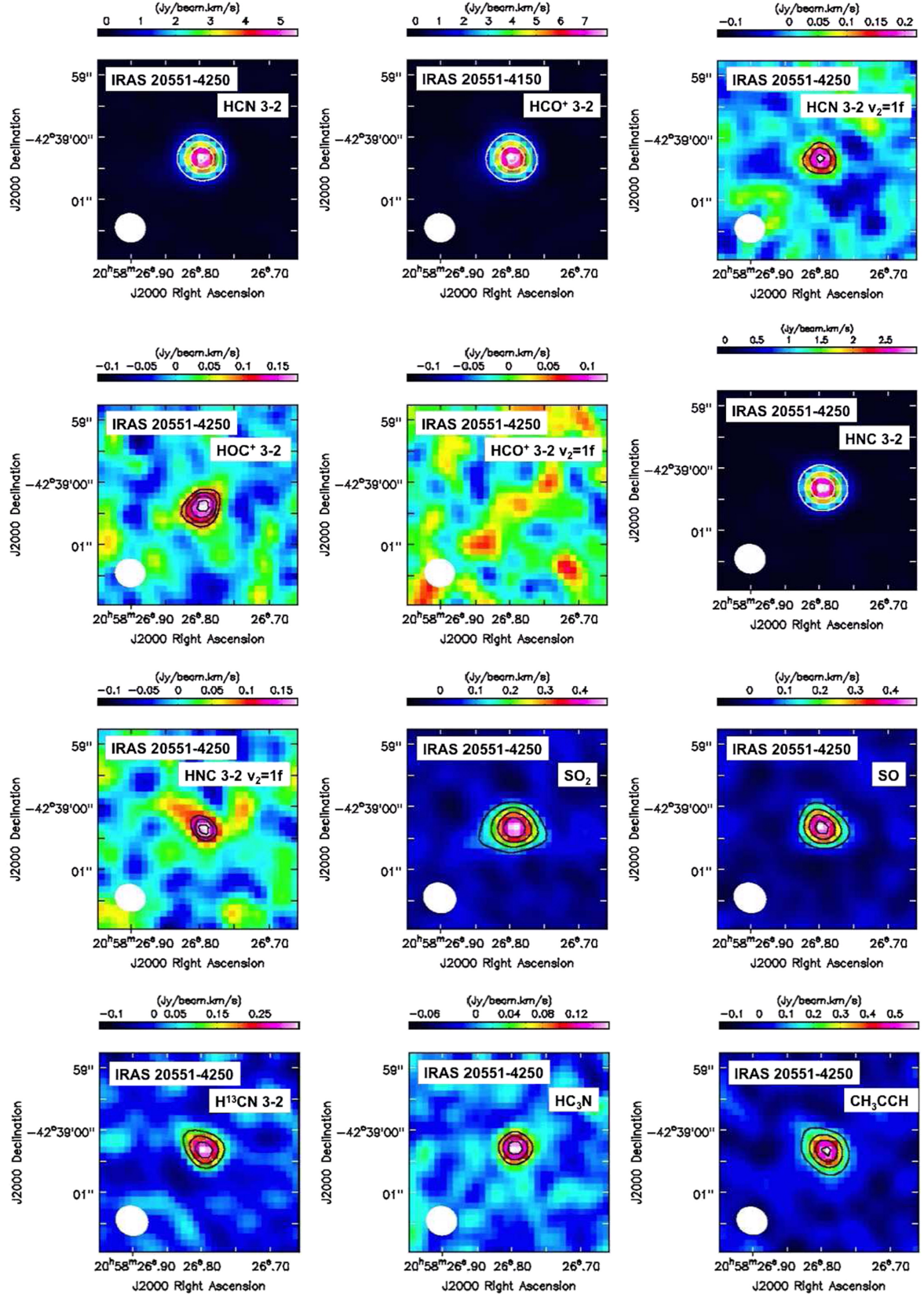
Figure 3. Integrated intensity (moment 0) maps of our interesting molecular lines in IRAS 20551−4250. The contours represent 20σ, 40σ, 60σ, 80σ for HCN $J = 3$–2; 20σ, 40σ, 60σ, 80σ for HCO$^+$ $J = 3$–2; 3σ, 5σ, 7σ for HCN $v_2 = 1$f $J = 3$–2; 3σ, 4σ, 5σ, 6σ for HOC$^+$ $J = 3$–2; 20σ, 40σ, 60σ, 80σ for HNC $J = 3$–2; 4σ, 5σ, 6σ for HNC $v_2 = 1$f $J = 3$–2; 4σ, 8σ, 12σ, 16σ for SO$_2$; 5σ, 10σ, 15σ, 20σ for SO; 4σ, 7σ, 10σ for H^{13}CN $J = 3$–2; 4σ, 6σ, 8σ for HC$_3$N; and 4σ, 8σ, 12σ, 16σ for CH$_3$CCH. For HCO$^+$ $v_2 = 1$f $J = 3$–2, no emission with $\geqq 3\sigma$ is found. The 1σ levels are different for different molecular lines. They are summarized in Table 3.

Table 3
Molecular Line Flux

Line	ν_{rest} (GHz)	Integrated Intensity (Moment 0) Map				Gaussian Line Fit			
		Peak (Jy beam^{-1} km s^{-1})	rms	Elements Summed	Beam ("×") (°)	Velocity (km s^{-1})	Peak (mJy)	FWHM (km s^{-1})	Flux (Jy km s^{-1})
(1)	(2)	(3)	(4)	(5)	(6)	(7)	(8)	(9)	(10)
HCN $J = 3$–2	265.89	5.5 (85σ)	0.064	16	0.49×0.46 (73°)	12894 ± 1	31 ± 1	187 ± 2	5.9 ± 0.1
HCO$^+$ $J = 3$–2	267.56	8.0 (87σ)	0.092	18	0.49×0.46 (75°)	12889 ± 1	43 ± 1	193 ± 2	8.4 ± 0.1
HCN $J = 3$–2, $v_2 = 1f$	267.20	0.22 (7.6σ)	0.029	9	0.49×0.46 (75°)	12883 ± 12	1.5 ± 0.2	165 ± 34	0.25 ± 0.07
HOC$^+$ $J = 3$–2	268.45	0.18 (6.4σ)	0.028	8	0.49×0.46 (74°)	12884 ± 21	1.4 ± 0.4	131 ± 55	0.19 ± 0.10
HCO$^+$ $J = 3$–2, $v_2 = 1f$	268.69	<0.088 (<3σ)	0.029	9	0.49×0.46 (74°)	...	...	...	...
HNC $J = 3$–2	271.98	3.0 (86σ)	0.035	14	0.50×0.47 (74°)	12895 ± 2	19 ± 1	164 ± 3	3.2 ± 0.1
HNC $J = 3$–2, $v_2 = 1f$ [a]	273.87	0.17 (6.5σ)	0.027	12	0.51×0.44 (66°)	12891 ± 29	0.80 ± 0.17	243 ± 68	0.20 ± 0.07
SO$_2$ 5(3,3)–5(2,4)	256.25	0.48 (20σ)	0.024	12	0.54×0.47 (65°)	12805 ± 5	3.1 ± 0.2	153 ± 12	0.49 ± 0.05
SO 6(6)–5(5)	258.26	0.48 (22σ)	0.021	11	0.53×0.47 (63°)	12912 ± 6	2.8 ± 0.2	188 ± 13	0.54 ± 0.05
H^{13}CN $J = 3$–2	259.01	0.34 (12σ)	0.028	15	0.53×0.47 (63°)	12884 ± 9	1.7 ± 0.2	205 ± 22	0.37 ± 0.05
HC$_3$N $J = 30$–29	272.89	0.16 (9.2σ)	0.017	8	0.50×0.47 (74°)	12900 ± 13	1.1 ± 0.2	166 ± 32	0.19 ± 0.05
CH$_3$CCH 16(2)–15(2)	273.40	0.59 (17σ)	0.034	17	0.51×0.44 (66°)	12866 ± 7	2.8 ± 0.2	203 ± 17	0.58 ± 0.06

Note. Col. (1): Observed molecular line. Molecular lines above the solid horizontal line were obtained simultaneously with continuum-a. Those below the line were taken at the same time as continuum-b. Col. (2): Rest-frame frequency of each molecular line in (GHz). Col. (3): Integrated intensity in (Jy beam^{-1} km s^{-1}) at the emission peak. Value at the highest flux pixel ($0''1$ pixel^{-1}) is extracted. Detection significance relative to the rms noise (1σ) in the moment 0 map is shown in parentheses. Possible systematic uncertainty is not included. Col. (4): rms noise (1σ) level in the moment 0 map in (Jy beam^{-1} km s^{-1}), derived from the standard deviation of sky signals in each moment 0 map. Col. (5): The number of spectral elements summed to create moment 0 maps. Each spectral element ($\sim$20 MHz width) consists of 40 correlator channels binning (see Section 2). Col. (6): Beam size in (arcsec × arcsec) and position angle in (°). Position angle is 0° along the north–south direction, and increases counterclockwise. Cols. (7)–(10): Gaussian fits of emission lines in the spectra at the continuum peak position, within the beam size. Col. (7): Optical LSR velocity (v_{opt}) of emission peak in (km s^{-1}). Col. (8): Peak flux in (mJy). Col. (9): Observed FWHM in (km s^{-1}) in Figure 4. Col. (10): Flux in (Jy km s^{-1}). Possible systematic uncertainty is not included. The observed FWHM in (km s^{-1}) in column 9 is divided by $(1 + z)$ to obtain the intrinsic FWHM in (km s^{-1}).
[a] HNC $v_2 = 1f$ $J = 3$–2 emission line could possibly be contaminated by HC$_3$N $v_7 = 1f$ $J = 30$–29 line ($\nu_{rest} = 273.94$ GHz; Costagliola et al. 2013). Although the peak velocity of the HNC $v_2 = 1f$ $J = 3$–2 emission line based on Gaussian fit is comparable to those of HCN, HCO$^+$, and HNC $v = 0$ $J = 3$–2 emission lines, as well as the HCN $v_2 = 1f$ $J = 3$–2 emission line, the line width is 25%–50% larger, possibly indicating contamination.

observations is included. These ratios are comparable to the expected ratio for thermally excited, optically thick gas ($= 16/9$), which suggests that the excitation temperatures of HCN, HCO$^+$, and HNC for $J = 3$–2 and $J = 4$–3 are comparable to the kinetic temperature of molecular gas in the nuclear region of IRAS 20551−4250. In general, when molecular gas density and temperature are not sufficiently high, collisional excitation at high J-levels can become sub-thermal more quickly and deviates from thermal condition more strongly for a molecule with a higher critical density than another molecule with lower critical density. While HCN and HNC have comparable critical densities at individual J-transitions, HCO$^+$ has a slightly lower critical density than HCN and HNC by a factor of $\sim$5 for the same J-transition (Meijerink et al. 2007; Greve et al. 2009). Thus, the HCN-to-HCO$^+$ flux ratio can be smaller at a higher J-transition (e.g., $J = 4$–3) than at a lower J-transition (e.g., $J = 3$–2) in some galaxies. The observed similar HCN-to-HCO$^+$ and HCN-to-HNC flux ratios between $J = 4$–3 and $J = 3$–2 suggest that the different excitation condition for different molecules (item (b) above) is not an important factor for the ratios at $J = 3$–2 and $J = 4$–3 in IRAS 20551−4250. However, in other galaxies, sub-thermal excitation conditions can occur, in which case the observed HCN-to-HCO$^+$ flux ratio at $J = 4$–3 (and $J = 3$–2) can be smaller than that at $J = 1$–0. This may be partly responsible for the small observed HCN-to-HCO$^+$ $J = 4$–3 flux ratios in starburst-dominated regions in Figure 6 (Imanishi & Nakanishi 2014). If this is the case, sufficient excitation at up to $J = 4$ in IRAS 20551−4250 contributes to its higher HCN-to-HCO$^+$ flux ratio at $J = 4$–3 (and $J = 3$–2) than starburst-dominated regions.

4.2. Vibrationally Excited HCN/HCO$^+$/HNC J = 3–2 Emission Lines

HCN, HCO$^+$, and HNC have three vibrational modes (v_1, v_2, and v_3). Since the energy level of $v_2 = 1$ is the lowest, its vibrational excitation is the simplest (Townes & Schawlow 1975; Amano 1983; Davies et al. 1984; Foster & McKellar 1984; Foster et al. 1984; Kawaguchi et al. 1985). The HCN $v_2 = 1f$ $J = 4$–3, $J = 3$–2, and HNC $v_2 = 1f$ $J = 3$–2 emission lines have previously been detected in the LIRG NGC 4418 ($L_{IR}\sim10^{11}L_\odot$; Sakamoto et al. 2010; Costagliola et al. 2013, 2015), which has observational signatures of a luminous buried AGN (Spoon et al. 2001; Evans et al. 2003; Imanishi et al. 2004; Sakamoto et al. 2013). The HCN $v_2 = 1f$ $J = 4$–3 emission line has also been detected in the AGN-hosting ULIRG, IRAS 20551−4250 ($L_{IR} \sim 10^{12}L_\odot$; Imanishi & Nakanishi 2013b). The other AGN-hosting ULIRG, Mrk 231 ($L_{IR} \sim 10^{12.5}L_\odot$; Sanders et al. 2003), also shows a detectable HCN $v_2 = 1f$ $J = 3$–2 emission line (Aalto et al. 2015b). Very recently, the detection of the HCN $v_2=1f$ $J = 3$–2 emission lines in three LIRGs (IC 860, Zw 049.057, and Arp 220) and HCN $v_2 = 1f$ $J = 4$–3 emission lines in two LIRGs (Arp 220W and IRAS 17208−0014) has been reported (Aalto et al. 2015a; Martin et al. 2016). This paper adds the detection of HCN $v_2 = 1f$ $J = 3$–2 and HNC $v_2 = 1f$ $J = 3$–2 emission lines in IRAS 20551−4250.

Regarding the HCO$^+$ $v_2 = 1f$ $J = 3$–2 emission line, we obtain a non-detection in our ALMA data for IRAS 20551 −4250 (Table 3). The HCO$^+$ $v_2 = 1f$ emission line has never been discussed in detail for external galaxies in the published
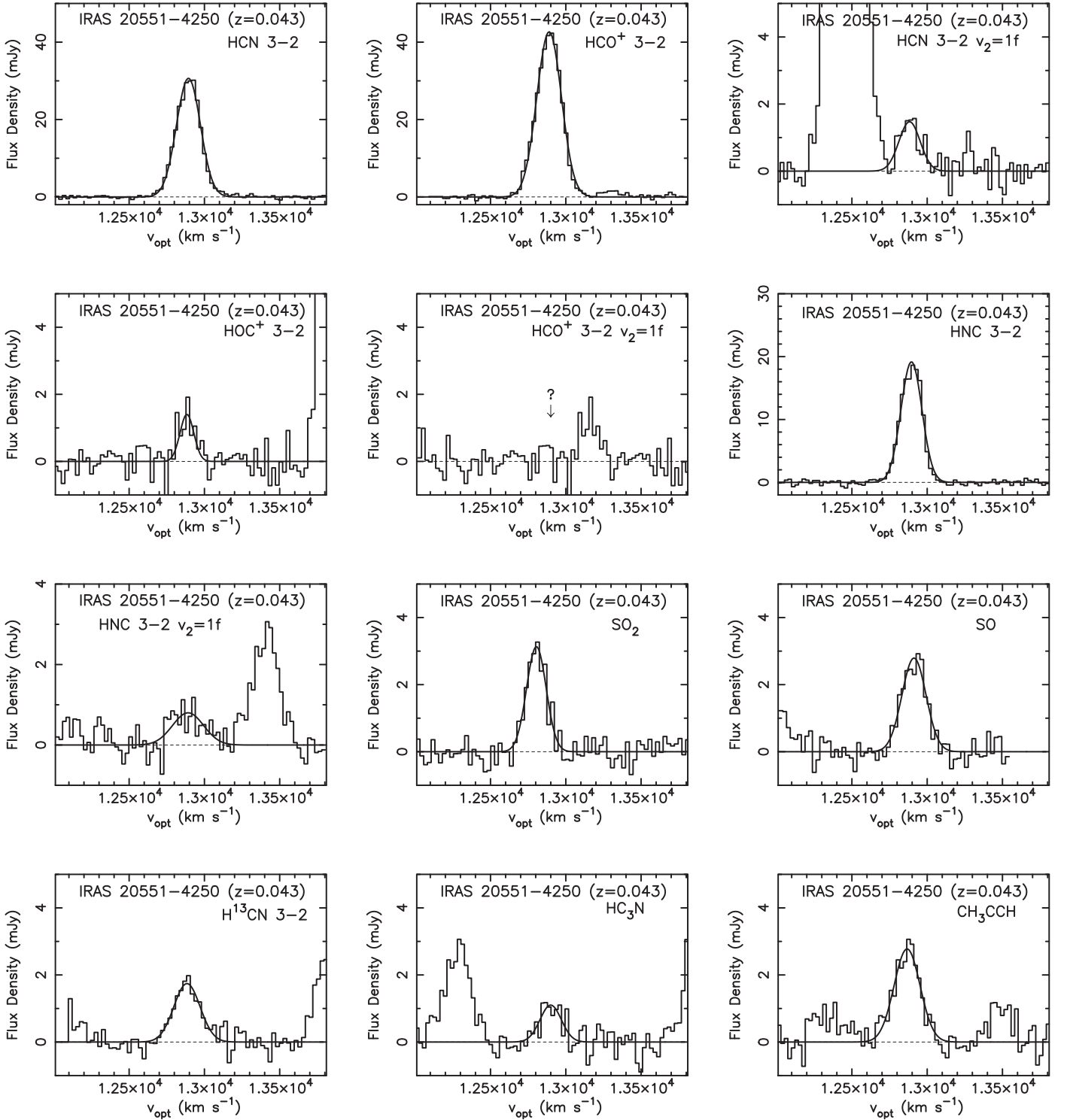
Figure 4. Spectra at the continuum peak position, within the beam size, of our interesting molecular lines in IRAS 20551−4250. All spectra are extracted at the continuum peak position at (20 58 26.80, −42 39 00.3) J2000. The abscissa is the optical LSR velocity ($v_{opt} \equiv c\,(\lambda - \lambda_0)/\lambda_0$), and the ordinate is the flux density in (mJy). The best Gaussian fits (Table 3) are overplotted as solid curved lines.

literature. Sakamoto et al. (2010) covered this HCO$^+$ $v_2 = 1f$ $J = 3$–2 emission line in the data of NGC 4418 and reported its non-detection with no upper limit flux provided. In the present paper, we provide the first stringent constraint on the upper limit of its flux in external galaxies.

In the case of optically thin conditions, the column density of the level u (N_u) is written as

$$N_u = \frac{4\pi}{hcA_{ul}\Omega} \times \text{flux} \qquad (1)$$

Table 4
Molecular Line Luminosity for IRAS 20551−4250

Line (1)	$(10^4 \, L_\odot)$ (2)	$(10^7 \, \mathrm{K \, km \, s^{-1} \, pc^2})$ (3)
HCN $J = 3$–2	5.5 ± 0.1	9.2 ± 0.2
HCO$^+$ $J = 3$–2	7.9 ± 0.1	12.9 ± 0.2
HNC $J = 3$–2	3.1 ± 0.1	4.7 ± 0.1
HCN $J = 3$–2 $v_2 = 1f$	0.23 ± 0.07	0.35 ± 0.10
HCO$^+$ $J = 3$–2 $v_2 = 1f$	<0.084	<0.13
HNC $J = 3$–2 $v_2 = 1f$	0.19 ± 0.07	0.27 ± 0.09
HCN $J = 4$–3	11.8 ± 0.3	8.3 ± 0.2
HCO$^+$ $J = 4$–3	17.5 ± 1.3	12.1 ± 0.9
HNC $J = 4$–3	7.4 ± 0.3	4.8 ± 0.2
HCN $J = 4$–3 $v_2 = 1f$	0.49 ± 0.09	0.34 ± 0.06

Note. Col. (1): Molecular line. Col. (2): Luminosity in units of $(10^4 \, L_\odot)$, calculated with Equation (1) of Solomon & Vanden Bout (2005). Col. (3): Luminosity in units of $(10^7 \, \mathrm{K \, s^{-1} \, pc^2})$, calculated with Equation (3) of Solomon & Vanden Bout (2005). Luminosities at $J = 4$–3 are also calculated from data by Imanishi & Nakanishi (2013b).

$$\propto \frac{\mathrm{flux}}{A_{ul}}, \qquad (2)$$

where the line flux from the upper (u) to lower (l) transition level is in units of $(\mathrm{Jy \, km \, s^{-1}})$, h is the Planck constant, c is the speed of light, Ω is the source solid angle, and A_{ul} is the Einstein A coefficient for spontaneous emission from the upper (u) to lower (l) level (Goldsmith & Langer 1999; Izumi et al. 2013). We assume that HCN, HCO$^+$, and HNC surround energy sources (buried AGN and stars) with an almost full covering factor in the same geometry, because (a) the optical spectroscopic non-Seyfert classification of IRAS 20551−4250 (Duc et al. 1997; Yuan et al. 2010) suggests that the putative AGN detected in infrared and X-ray observations (Section 1) is obscured by dust and molecular gas in virtually all directions (buried), and (b) newly formed stars are also deeply embedded in dust and molecular gas. Namely, the emission structure inside the ALMA synthesized beam is assumed to be the same among HCN, HCO$^+$, and HNC. Adopting the Einstein A coefficients from the $J = 3$ to $J = 2$ level at $v_2 = 1f$ shown in Table 5, the ratio of the column density at the $v_2 = 1f \, J = 3$ level among HCN, HCO$^+$, and HNC is

$$\mathrm{HCN : HCO^+ : HNC} (N_{v_2 = 1f, J = 3}) \, \mathrm{(observed)}$$
$$= 1 : <0.20 : 0.69, \qquad (3)$$

where the fluxes based on Gaussian fits (Table 3, column 10) are used for the detected HCN $v_2 = 1f \, J = 3$–2 and HNC $v_2 = 1f \, J = 3$–2 lines, whereas the upper limit ($<3\sigma$) in the integrated intensity (moment 0) map (Table 3, column 3) is adopted for the undetected HCO$^+$ $v_2 = 1f \, J = 3$–2 line. This will be compared to theoretical calculations in the following subsection. If the HC$_3$N $v_7 = 1f \, J = 30$–29 emission blends with HNC $v_2 = 1f \, J = 3$–2 (Costagliola et al. 2013), the actual HNC $v_2 = 1f \, J = 3$–2 emission line flux could be smaller by 25%–50% (Table 3).

The ratios of observed $v_2 = 1f \, J = 3$–2 to $v = 0 \, J = 3$–2 flux in units of $(\mathrm{Jy \, km \, s^{-1}})$ for HCN, HCO$^+$, and HNC are

summarized in Table 6. The ratios are

$$\mathrm{HCN : HCO^+ : HNC} (v_2 = 1f / v = 0) \, \mathrm{(observed)}$$
$$= 1 : <0.25 : 1.5. \qquad (4)$$

This is the second observed quantity to indicate the efficiency of vibrational excitation to the $v_2 = 1$ level.

4.3. Comparison with the Infrared Radiative Pumping Model

4.3.1. Abundance Ratio among HCN, HCO$^+$, and HNC

The energy levels of $v_2 = 1$ are ∼1030 K (HCN), ∼1200 K (HCO$^+$), and ∼670 K (HNC). These energy levels are too high to be collisionally excited, but could be excited by infrared radiative pumping by absorbing infrared photons at ∼14 μm (HCN), ∼12 μm (HCO$^+$), and ∼21.5 μm (HNC). The ratio in Equation (3) reflects the product of the infrared radiative pumping rate to $v_2 = 1$ and column density at $v = 0$ of each molecule. To estimate the effect of the infrared radiative pumping, we assume that (a) HCN, HCO$^+$, and HNC emission lines at both $v = 0$ and $v_2 = 1f$ come from the same regions relative to the central buried AGN of IRAS 20551−4250, and (b) the column density at $v = 0$ ($N_{v = 0}$) is comparable among HCN, HCO$^+$, and HNC. The first assumption comes from the fact that HCN, HCO$^+$, and HNC have similar dipole moments ($\mu = 3.0$, 3.9, and 3.1 Debye, respectively), and so their emission lines at the same J-transition at $v = 0$ probe similarly dense molecular gas in a galaxy compared to the widely used CO J-lines ($\mu = 0.1$ Debye), which trace much less dense molecular gas at the same J-transition. Here, it is assumed that $v_2 = 1f$ emission also comes from the same regions. These assumptions will be discussed later.

The infrared radiative pumping rate (P_{IR}) is

$$P_{\mathrm{IR}} \propto B_{v_2 = 0-1, \mathrm{vib}} \times F_{\nu (\mathrm{IR})} \times N_{v=0}, \qquad (5)$$

where $B_{v2 = 0-1, \mathrm{vib}}$ is the Einstein B coefficient from $v = 0$ to $v_2 = 1$, $F_{\nu \, (\mathrm{IR})}$ is infrared flux in F_ν (Jy) used for the infrared radiative pumping of HCN/HCO$^+$/HNC, and $N_{v = 0}$ is the column density at the $v = 0$ level. The $B_{v2 = 0-1, \mathrm{vib}}$ is related to the Einstein A coefficient from $v_2 = 1$ to $v = 0$ ($A_{v2 = 1-0, \mathrm{vib}}$) in the form of

$$B_{v_2 = 0-1, \mathrm{vib}} \propto \lambda^3 \times A_{v_2 = 1-0, \mathrm{vib}} \qquad (6)$$

(Rybicki & Lightman 1979).

For $v_2 = 1$, the $A_{v2 = 1-0, \mathrm{vib}}$ values are estimated to be ∼1.7 s^{-1} (HCN) (Deguchi et al. 1986; Aalto et al. 2007), ∼3.0 s^{-1} (HCO$^+$; Mauclaire et al. 1995), and ∼5.2 s^{-1} (HNC; Aalto et al. 2007). Thus, the ratio of the $B_{v2 = 0-1, \mathrm{vib}}$ value among HCN, HCO$^+$, and HNC is

$$\mathrm{HCN : HCO^+ : HNC} (B_{v_2 = 0-1, \mathrm{vib}}) = 1 : 1.1 : 11. \qquad (7)$$

The infrared flux for the infrared radiative pumping of HCN (14 μm), HCO$^+$ (12 μm), and HNC (21.5 μm) is estimated from the 5–35 μm spectrum of IRAS 20551−4250 taken by the *Spitzer* IRS (Figure 7). The 5–35 μm spectrum in Figure 7 shows strong silicate dust absorption features at $\lambda_{\mathrm{rest}} \sim 9.7$ μm and 18 μm (rest frame), which means that mid-infrared (3–20 μm) continuum emission originated in energy sources (buried AGNs and/or stars) is obscured by dust at the foreground. We need to correct for these silicate dust absorption features if we are to obtain the intrinsic mid-infrared spectral energy distribution which is produced in the
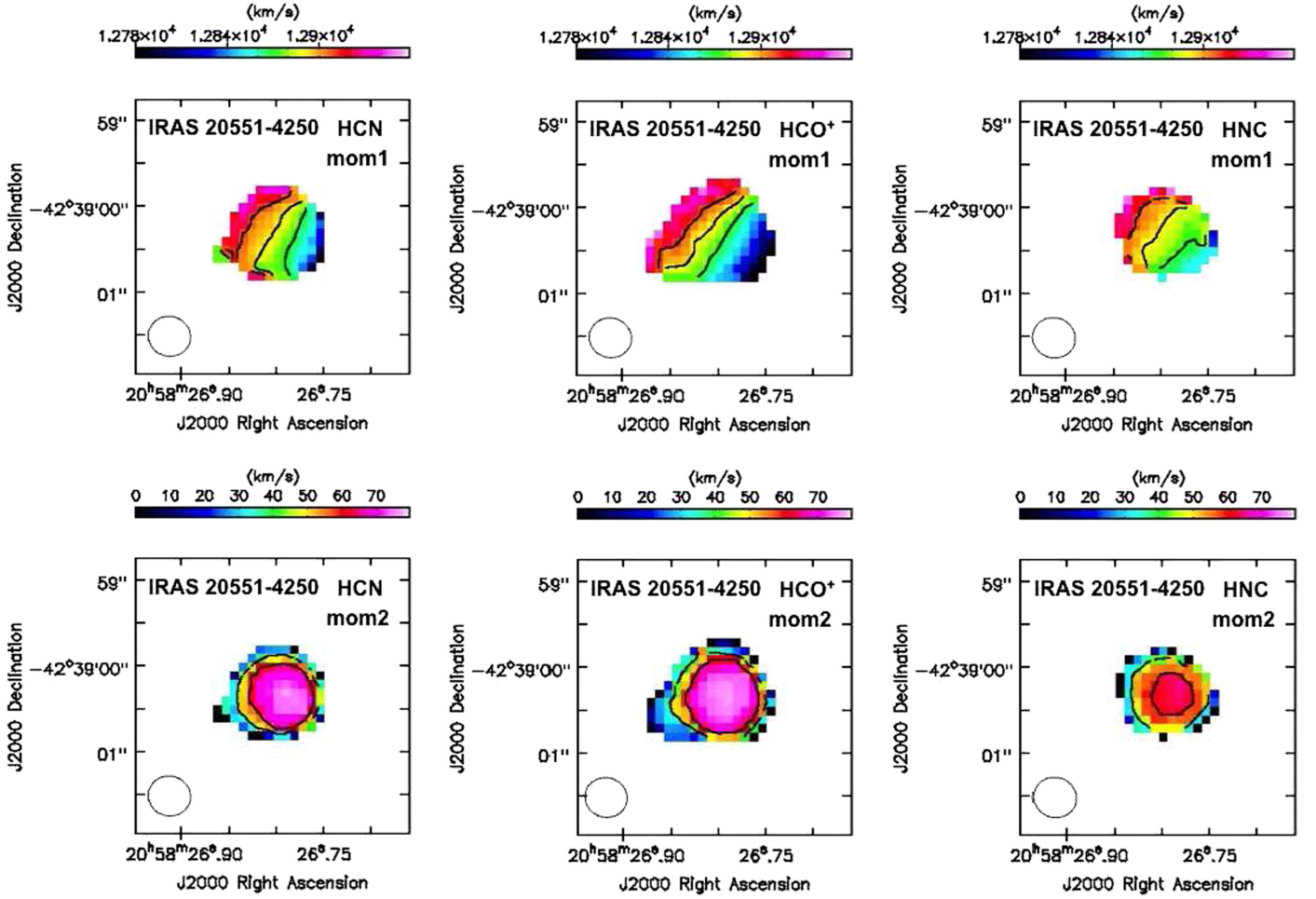
Figure 5. Intensity-weighted mean velocity (moment 1) and intensity-weighted velocity dispersion (moment 2) maps of the HCN/HCO$^+$/HNC $J = 3$–2 ($v = 0$) emission lines for IRAS 20551$-$4250. For moment 1 maps (top panels), the velocity is in optical LSR velocity ($v_{opt} \equiv c\,(\lambda - \lambda_0)/\lambda_0$). The contours in moment 1 maps are 12870, 12890, and 12910 km s^{-1} for HCN/HCO$^+$/HNC $J = 3$–2. The contours in moment 2 maps (bottom panels) are 40 and 60 km s^{-1} for HCN/HCO$^+$/HNC $J = 3$–2.

close vicinity of the obscured energy sources and is illuminated to their nearby molecular gas.

The HCN $v_2 = 1f$ $J = 3$–2 or $J = 4$–3 emission was detected in some Galactic sources (Ziurys & Turner 1986; Mills et al. 2013; Veach et al. 2013; Nagy et al. 2015). Since the emission can be produced in the region where infrared 14 μm photons are available and since Galactic sources emit some amount of infrared 14 μm photons, the detection in nearby Galactic sources is reasonable, as long as observations are sensitive enough to detect low-luminosity emission. However, IRAS 20551$-$4250 at $z = 0.043$ (luminosity distance is 188 Mpc) is much further away from our Galaxy and the detected $v_2 = 1f$ emission line luminosity in IRAS 20551$-$4250 (Table 4) is more than several orders of magnitude higher than the Galactic sources. Since an AGN is a much stronger mid-infrared continuum emitter than a starburst under the same bolometric luminosity, due to the larger amount of hot dust in the former (Section 1), an AGN can produce strong $v_2 = 1f$ emission more easily than stars. Nardini et al. (2008, 2009) estimated that ~90% of the observed 5–8 μm flux of IRAS 20551$-$4250 comes from AGN-heated hot dust emission. We also investigate the rest-frame equivalent widths of the 6.2, 7.7, and 11.3 μm polycyclic aromatic hydrocarbon (PAH) emission features from the spectrum of IRAS 20551$-$4250 in Figure 7,

using the same definition as that employed by Imanishi et al. (2007a). It is widely accepted that a starburst shows strong PAH emission features, while a pure AGN does not (Moorwood 1986; Genzel et al. 1998; Imanishi & Dudley 2000), because PAHs are destroyed in the close vicinity of an AGN (Voit 1992). The derived rest-frame equivalent widths of the 6.2 μm, 7.7 μm, and 11.3 μm PAH emission features are ~45 (nm), ~190 (nm), and ~185 (nm), respectively. These values are much smaller than the typical values found in starburst-dominated galaxies (~540 (nm), ~690 (nm), and ~600 (nm) for the 6.2 μm, 7.7 μm, and 11.3 μm PAH emission features, respectively; Imanishi et al. 2007a), which again supports the scenario that the observed mid-infrared flux of this galaxy is dominated by AGN-heated hot dust emission. Farrah et al. (2003) also modeled that the observed 10–25 μm emission of IRAS 20551$-$4250 is dominated by an AGN-origin dust continuum emission component. Thus, we regard that the observed mid-infrared continuum from IRAS 20551$-$4250 is dominated by the AGN-heated hot dust emission. Since the AGN-heated hot dust emission is spatially very compact and is more centrally concentrated than surrounding dust (Imanishi et al. 2007a), a simple foreground screen dust model is applicable.
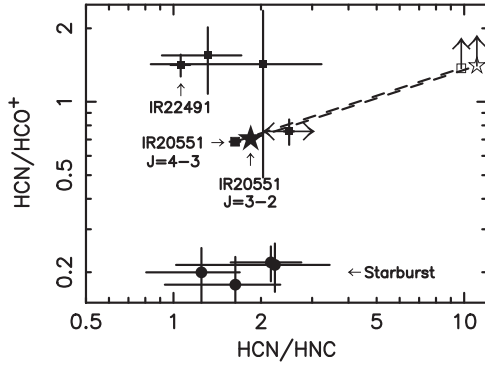
Figure 6. Observed HCN-to-HNC (abscissa) and HCN-to-HCO$^+$ (ordinate) flux ratios based on ALMA observations. The filled circles are $J = 4$–3 data at multiple positions of the starburst-dominated LIRG NGC 1614 taken by ALMA Cycle 0 observations (Imanishi & Nakanishi 2013a). The filled squares are $J = 4$–3 data of ULIRGs taken by ALMA Cycle 0 observations (Imanishi & Nakanishi 2013b, 2014). Although the ratios are unchanged, uncertainties are recalculated. All ULIRGs but one (IRAS 22491−1808) show infrared-identified energetically important buried AGNs (Imanishi & Nakanishi 2014). For IRAS 22491−1808, the HCN $v_2 = 1f$ $J = 3$–2 emission line has been detected in our ALMA Cycle 2 data (Imanishi 2016), suggesting that this ULIRG may contain an extremely buried AGN which is infrared-elusive but (sub)millimeter-detectable. The filled star is our new ALMA Cycle 2 $J = 3$–2 data of IRAS 20551−4250. For IRAS 20551−4250, ratios after the correction for the derived line opacities (Section 4.3.2) are shown as the open square ($J = 4$–3) and open star ($J = 3$–2), which are connected to the observed ratios with the dashed lines.

Table 5
Parameters for Molecular Transition Lines

Line	Frequency (GHz)	E_u/k_B (K)	A_{ul} (10^{-4} s^{-1})	Flux (Jy km s^{-1})
(1)	(2)	(3)	(4)	(5)
HCN $J = 3$–2	265.89	25.5	8.4	5.9 ± 0.1
HCN $J = 3$–2, $v_2 = 1f$	267.20	1050.0	7.3	0.25 ± 0.07
HCO$^+$ $J = 3$–2	267.56	25.7	14.5	8.4 ± 0.1
HCO$^+$ $J = 3$–2, $v_2 = 1f$	268.69	1217.4	13.1	<0.088
HNC $J = 3$–2	271.98	26.1	9.3	3.2 ± 0.1
HNC $J = 3$–2, $v_2 = 1f$	273.87	692.0	8.5	0.20 ± 0.07
HCN $J = 4$–3	354.51	42.5	20.6	9.5 ± 0.2
HCN $J = 4$–3, $v_2 = 1f$	356.26	1067.1	19.0	0.39 ± 0.07

Note. Col. (1): Transition line. Col. (2): Rest-frame frequency in (GHz). Col. (3): Upper energy level in (K). Col. (4): Einstein A coefficient for spontaneous emission in (10^{-4} s^{-1}). Values in Cols. (3) and (4) are from the Cologne Database of Molecular Spectroscopy (CDMS) (Müller et al. 2005) via Splatalogue (http://www.splatalogue.net). Col. (5): Flux in (Jy km s^{-1}) estimated based on Gaussian fits (Table 3, column 10). For the undetected HCO$^+$ $v_2 = 1f$ $J = 3$–2 emission line, an upper limit based on the integrated intensity (moment 0) map is adopted. HCN $J = 4$–3 fluxes at $v_2 = 1f$ and $v = 0$ are from Imanishi & Nakanishi (2013b).

Following Imanishi et al. (2007a), we adopt power-law-shaped intrinsic continua, using data unaffected by the silicate dust absorption features and strong PAH emission features. The derived intrinsic power-law continua, after correcting for the silicate dust absorption features using the foreground screen dust model, are shown in Figure 7. The ratio of the infrared flux

used for the infrared radiative pumping among HCN (14 μm), HCO$^+$ (12 μm), and HNC (21.5 μm) is

$$\text{HCN: HCO}^+\text{: HNC}(F_{\nu(\text{IR})}) = 1: 0.8: 2.5, \qquad (8)$$

where we compare the power-law continuum fluxes at the redshifted wavelengths with $z = 0.043$. The infrared spectral energy distribution of the hidden energy source of IRAS 20551 −4250 (in F_ν) shows higher fluxes with increasing wavelength at 5–35 μm. Strictly speaking, the continuum emission outside the strong silicate dust absorption features could be flux-attenuated by foreground dust absorption, and its shape could change slightly. However, as we will show below, this change is insignificant. The optical depth of the 9.7 μm silicate dust absorption feature relative to the adopted power-law continuum level in Figure 7 is estimated to be $\tau_{9.7} \sim 2.7$. This corresponds to $A_V = 25$–50 mag, if the relation of $\tau_{9.7}/A_V = 0.054$–0.11 found in the Galactic interstellar medium (Roche & Aitken 1984, 1985) is adopted. The dust extinction at 5–20 μm, outside the strong silicate dust absorption features (A_{MIR}), is $A_{\text{MIR}} = 0.027 \times A_V$ (Nishiyama et al. 2008, 2009), or $A_{\text{MIR}} = 0.7$–1.4 mag in the case of IRAS 20551−4250. Since the dust extinction curve at 5–20 μm is relatively flat (Fritz et al. 2011), the possible change in the intrinsic continuum spectral shape at 5–20 μm outside the silicate dust absorption features, through dust extinction, is too small to significantly affect our discussion. Thus, we adopt the ratio of Equation (8).

Adopting the above values, the ratio of the infrared radiative pumping rate among HCN, HCO$^+$, and HNC is

$$\text{HCN: HCO}^+\text{: HNC}(P_{\text{IR}})(\text{predicted}) = 1: 0.9: 27. \qquad (9)$$

Namely, the infrared radiative pumping rate of HNC is much higher than those for HCN and HCO$^+$, mainly due to the longer wavelength of the infrared $v_2 = 1$ absorption line. The Einstein A coefficient for the rotational $J = 3$–2 transition at $v_2 = 1f$ ($A_{J=3-2,\text{rot},v_2=1f}$), relative to that for the vibrational transition from $v_2 = 1$ to $v = 0$ ($A_{v_2=1-0,\text{vib}}$), is $\sim 4 \times 10^{-4}$, $\sim 4 \times 10^{-4}$, and $\sim 2 \times 10^{-4}$ for HCN, HCO$^+$, and HNC, respectively (Table 5 and Section 4.3.1, third paragraph). Thus, most of the vibrationally excited molecules to $v_2 = 1$ quickly decay back to $v = 0$ rather than decaying to a lower rotational J-level at $v_2 = 1$. However, the $A_{J=3-2,\text{rot},v_2 = 1f}$ to $A_{v_2 = 1-0,\text{vib}}$ ratios agree within a factor of ~ 2 among HCN, HCO$^+$, and HNC. Once vibrationally excited to $J = 3$ at $v_2 = 1f$, a similar fixed fraction of rotational J-transition from $J = 3$ to $J = 2$ at $v_2 = 1f$ is expected, which should be detectable as the $v_2 = 1f$ $J = 3$–2 emission line. Thus, the detection of the HNC $v_2 = 1f$ $J = 3$–2 emission line in a galaxy with detectable HCN $v_2 = 1f$ $J = 3$–2 and $J = 4$–3 emission lines is quite reasonable under our current assumption that HCN and HNC have comparable column density at $v = 0$. On the other hand, the radiative pumping rates of HCN and HCO$^+$ are comparable. The detection of the HCN $v_2 = 1f$ $J = 3$–2 emission line, without the detection of the HCO$^+$ $v_2 = 1f$ $J = 3$–2 emission line, requires some consideration.

When the $v_2 = 1$ to $v = 0$ column density ratio ($N_{v_2=1}/N_{v = 0}$), controlled by the infrared radiative pumping, is $\ll 1$ (see Section 4.5), we obtain the relation

$$N_{v=0} \times B_{v_2=0-1,\text{vib}} \times F_{\nu(\text{IR})} = N_{v_2=1} \times A_{v_2=1-0,\text{vib}}. \qquad (10)$$

Table 6
$v_2 = 1f$ to $v = 0$ Flux Ratio

Object (1)	Line (2)	Observed Ratio (3)	Flux Attenuation (4)	Intrinsic Ratio (5)	Reference (6)
IRAS 20551−4250	HCN $J = 3$–2	0.042	6	~0.01	This work
	HCO$^+$ $J = 3$–2	<0.011	<3	<0.01	This work
	HNC $J = 3$–2	0.063	~1	~0.06	This work
	HCN $J = 4$–3	0.041	6	~0.01	Imanishi & Nakanishi (2013b)
NGC 4418	HCN $J = 4$–3	0.23	~20	~0.01	Sakamoto et al. (2010)
	HCN $J = 3$–2	0.17	~20	~0.01	Sakamoto et al. (2010)
Mrk 231	HCN $J = 3$–2	0.042	~10	~0.005	Aalto et al. (2015b)

Note. Col. (1): Object name. Only LIRGs with available quantitative information of flux attenuation for $v = 0$ emission are shown. Col. (2): Molecular transition line. Col. (3): Ratio of the observed $v_2 = 1f$ to $v = 0$ emission line flux in (Jy km s^{-1}). Col. (4): Estimated flux attenuation for $v = 0$ emission. The value of 6 means that flux is attenuated by line opacity with a factor of 6. Col. (5): Ratio of the intrinsic $v_2 = 1f$ to $v = 0$ emission line flux in (Jy km s^{-1}), after line opacity correction of $v = 0$ emission. Col. (6): Reference.
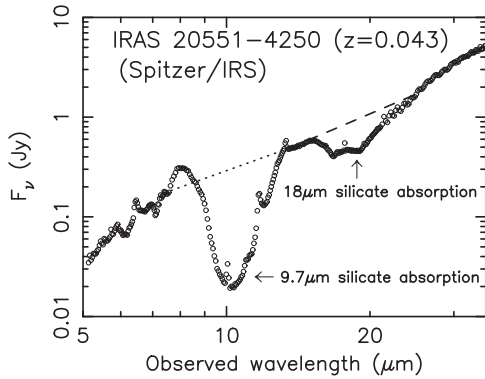
Figure 7. *Spitzer* IRS low-resolution ($R \sim 100$) infrared 5–35 μm spectrum of IRAS 20551−4250, originally shown by Imanishi et al. (2011), analyzed in the same manner as described in our previously published *Spitzer* IRS papers (Imanishi et al. 2007a, 2010a; Imanishi 2009). It is virtually identical to the spectrum shown by Sargsyan et al. (2011), except for small gaps among different spectral modules in the latter. The adopted power-law continuum level for the 9.7 μm (18 μm) silicate dust absorption feature is determined based on data points not strongly affected by these absorption features and polycyclic aromatic hydrocarbon (PAH) emission features (Imanishi et al. 2007a), and is overplotted as the dotted (dashed) line.

Here, transitions among rotational J-levels within $v = 0$ and $v_2 = 1$ are neglected. From this equation, we obtain

$$\frac{N_{v_2=1}}{N_{v=0}} = \frac{B_{v_2=0-1,\mathrm{vib}} \times F_{\nu(\mathrm{IR})}}{A_{v_2=1-0,\mathrm{vib}}} \quad (11)$$

$$\propto \lambda^3 \times F_{\nu(\mathrm{IR})}, \quad (12)$$

where the relation in Equation (6) is used. Thus, the $v_2 = 1$ to $v = 0$ column density ratios among HCN, HCO$^+$, and HNC are

$$\mathrm{HCN:\ HCO^+:\ HNC}(N_{v_2=1}/N_{v=0})(\text{predicted}) = 1:0.5:9. \quad (13)$$

We note that Ziurys & Turner (1986) adopt a higher $A_{v2 = 1-0,}$ $_{\mathrm{vib}}$ value of 3.7 s^{-1} for HCN than our assumption (1.7 s^{-1}). However, this predicted column density ratio is independent of the absolute $A_{v2 = 1-0,\mathrm{vib}}$ values of HCN, HCO$^+$, HNC because of the division of $B_{v2 = 0-1,\mathrm{vib}}$ by $A_{v2 = 1-0,\mathrm{vib}}$, as shown in Equations (11) and (12) Thus, the predicted ratio is robust to the possible uncertainty of the absolute $A_{v2 = 1-0,\mathrm{vib}}$ values of HCN, HCO$^+$, and HNC.

The observed $J = 4$–3 to $J = 3$–2 flux ratios in Section 4.1 suggest that HCN, HCO$^+$, and HNC are almost thermally excited and so are similarly populated at $J = 3$ and $J = 4$ at $v = 0$. Assuming that the fraction of $J = 3$ level, relative to all J-levels at $v = 0$, is similar among HCN, HCO$^+$, and HNC, Equations (3) (observation) and (13) (prediction) can be compared if the column density at $v = 0$ (and thereby abundance, which is proportional to the column density) is the same among HCN, HCO$^+$, and HNC. The discrepancy between the observation (Equation (3)) and prediction (Equation (13)) can be reconciled if the column density at $v = 0$ ($N_{v = 0}$) for HCN is higher than HCO$^+$ and HNC by factors of >2.5 and 13, respectively, where HCN/HCO$^+$/HNC $v_2 = 1f$ J-transition emission is assumed to be optically thin. Namely, the HCN-to-HCO$^+$ abundance ratio of >2.5 and HCN-to-HNC abundance ratio of 13 are suggested for the IRAS 20551−4250 nucleus. The HCN-to-HNC abundance ratio could be even higher if the HNC $v_2 = 1f$ $J = 3$–2 emission line flux is contaminated by HC$_3$N $v_7 = 1f$ $J = 30$–29 line (Table 3). In summary, we obtain the abundance ratio of

$$\mathrm{HCN:\ HCO^+:\ HNC}(\text{abundance}) = 1:<0.4:<0.08. \quad (14)$$

The higher abundance (and thereby higher column density at $v = 0$) of HCN than HCO$^+$ and HNC, derived in Equation (14), can naturally explain the following observational results that (a) HCN $v_2 = 1f$ $J = 3$–2 emission line is detected, without HCO$^+$ $v_2 = 1f$ $J = 3$–2 emission line detection, despite the similar infrared radiative pumping rate to the $v_2 = 1$ level (Equation (9)), and (b) the $v_2 = 1f$ $J = 3$–2 emission line fluxes are similar between HCN and HNC (Table 5), despite the much higher predicted infrared radiative pumping rate to $v_2 = 1$ in HNC than HCN (Equation (9)). Given that the bulk of the mid-infrared photons used for the vibrational excitation of HCN/HCO$^+$/HNC is interpreted to originate from AGN-heated hot dust thermal radiation, the properties of molecular gas derived from the $v_2 = 1f$ emission lines (i.e., higher abundance of HCN than HCO$^+$ and HNC) should reflect those of AGN-affected molecular gas in the close vicinity of an AGN.

In our Milky Way Galaxy, the HCN-to-HCO$^+$ abundance ratio is estimated to be 1.2 ± 0.4 in infrared dark clouds, based on molecular emission line studies (Liu et al. 2013) and 1.9 ± 0.9 in diffuse interstellar medium, based on molecular

absorption line studies (Godard et al. 2010). However, it has been suggested from observations and their interpretations that the HCN-to-HCO$^+$ abundance ratio is high in molecular gas in the close vicinity of AGNs (Yamada et al. 2007; Izumi et al. 2016). Thus, the derived HCN-to-HCO$^+$ abundance ratio with >2.5 at the IRAS 20551−4250 nucleus would be possible.

With respect to HCN and HNC, in our Galaxy, the abundance of HCN and HNC are comparable in cold dark clouds (Hirota et al. 1998; Liu et al. 2013; Graninger et al. 2014). However, in high-temperature clouds around active regions, the HNC abundance decreases by more than an order of magnitude relative to the HCN abundance (Schilke et al. 1992; Hirota et al. 1998; Graninger et al. 2014). Given that the bulk of HCN and HNC $J = 3$–2 emission at $v_2 = 1$ and $v = 0$ detected in the ALMA data for IRAS 20551−4250 come from nuclear active regions (Section 3), the increase in the HCN-to-HNC abundance ratio by more than an order of magnitude could occur.

Summarizing, our results suggest that in the nuclear region of IRAS 20551−4250, the HCN-to-HCO$^+$ and HCN-to-HNC abundance ratios are >2.5 and >10, respectively, which is quite possible based on previously obtained observational data from our own Galaxy and other galaxies.

The HCN $v_2 = 1f$ $J = 3$–2 or $J = 4$–3 emission lines were detected in some Galactic objects and star-forming regions despite much lower luminosity than IRAS 20551−4250 (Ziurys & Turner 1986; Mills et al. 2013; Veach et al. 2013; Nagy et al. 2015). However, the relative strengths of HCO$^+$ and HNC $v_2 = 1f$ $J = 3$–2 or $J = 4$–3 emission lines are not known, except for the luminous active star-forming region W49A, in which the $v_2 = 1f$ $J = 4$–3 emission line was detected for HCN and HNC but not for HCO$^+$ with no flux upper limit provided (Nagy et al. 2015). Infrared 5–14.5 μm spectra were taken at some offset regions in the vicinity of the W49A center (Stock et al. 2014), but are not available at the W49A center where the $v_2 = 1f$ $J = 4$–3 emission lines of HCN and HNC are detected (Nagy et al. 2015). Thus, the same analysis to derive molecular abundance ratios as that made for IRAS 20551−4250 in the earlier part of this section is currently not applicable to the W49A center and other Galactic sources with detectable HCN $v_2 = 1f$ emission lines. It might be possible that some specific Galactic stellar populations show an enhanced HCN abundance in their vicinity, despite the fact that a modest HCN-to-HCO$^+$ abundance ratio (=1.9 ± 0.9) is derived based on absorption studies of Galactic sources (Godard et al. 2010), which probe the ratio in a larger Galactic physical scale, in front of the background continuum-emitting sources, than emission-based abundance measurements.

There is an observational trend that the observed HCN-to-HCO$^+$ flux ratios in AGNs are higher than starburst galaxies (Section 1). The observed HCN-to-HCO$^+$ $J = 4$–3 flux ratio at the W49A center is also low, only ∼0.4 (Nagy et al. 2015). High observed HCN-to-HCO$^+$ flux ratios at $J = 4$–3 or $J = 3$–2 are produced not only by high HCN-to-HCO$^+$ abundance ratios, but also by sufficient excitation to $J = 4$ and 3, particularly for HCN due to its higher critical density than HCO$^+$ (Section 4.1). Since excitation to $J = 4$ or 3 is more efficiently achieved in an AGN than star formation because of an AGN's much higher radiative energy generation efficiency (Section 1), buried AGN selection based on high HCN-to-HCO$^+$ flux ratios remains effective. Since an AGN is expected to show a higher mid-infrared 14 μm to infrared (8–1000 μm)

luminosity ratio than star formation due to AGN-heated hot dust (Section 1), the HCN $v_2 = 1f$ $J = 4$–3 to infrared luminosity ratio in IRAS 20551−4250 is expected to be even higher than that in W49A if IRAS 20551−4250 indeed contains a luminous buried AGN. For W49A, adopting the infrared luminosity of >$10^7 L_\odot$ and a distance of 11 kpc (Nagy et al. 2015), the HCN $v_2 = 1f$ $J = 4$–3 to infrared luminosity ratio is <1.2 × 10^{-9}. The ratio for IRAS 20551−4250 is estimated to be 4.9 × 10^{-9} based on the infrared luminosity of $L_{IR} = 10^{12.0} L_\odot$ (Section 1) and observed HCN $v_2 = 1f$ $J = 4$–3 luminosity (Table 4). This ratio is more than a factor of four higher than W49A, supporting the strong AGN contributions to molecular gas emission at the IRAS 20551−4250 nucleus.

4.3.2. Flux Attenuation of HCN/HCO$^+$/HNC v = 0 J = 3–2 Emission

In Equation (4), because the Einstein A coefficient for spontaneous emission from $J = 3$ to $J = 2$ is almost identical between $v = 0$ and $v_2 = 1f$ (Table 5), the ratio is roughly converted into the column density ratio at $v_2 = 1f$ $J = 3$ and $v = 0$ $J = 3$ (see Equation (2)), provided that the opacity of $v = 0$ $J = 3$–2 emission is insignificant. In other words, the ratios in Equations (4) and (13) can be used to estimate the opacity of $v = 0$ $J = 3$–2 emission for HCN, HCO$^+$, and HNC. From this comparison, we derive that the flux attenuation of HCN $v = 0$ $J = 3$–2 emission is a factor of >2 larger than that of the HCO$^+$ $v = 0$ $J = 3$–2 emission, and is a factor of 6 larger than that of the HNC $v = 0$ $J = 3$–2 emission.

The observed HCN $J = 3$–2 to H^{13}CN $J = 3$–2 flux ratio is ∼16 (Table 3). The ^{12}C/^{13}C abundance ratios in starburst galaxies are estimated to be ∼50 (Henkel & Mauersberger 1993; Henkel et al. 1993, 2014) or possibly even higher (Martin et al. 2010). In ULIRGs, the ^{12}C/^{13}C abundance ratios are as high as ∼100 (Henkel et al. 2014). Assuming optically thin emission for H^{13}CN $J = 3$–2, HCN $J = 3$–2 emission is estimated to be optically thick, and its flux can be attenuated by a factor of 3–6. In this case, the flux attenuation of HNC $v = 0$ $J = 3$–2 emission becomes 0.5 (if the flux attenuation of HCN $v = 0$ $J = 3$–2 emission is 3) or 1 (if that of HCN $v = 0$ $J = 3$–2 emission is 6). Since the flux attenuation factor by line opacity is, by definition, always larger than unity, we adopt the flux attenuation of HCN $J = 3$–2 emission to be 6, which provides the flux attenuation of HCO$^+$ $v = 0$ $J = 3$–2 emission to be <3.

According to the widely accepted model of molecular gas in galaxies, molecular clouds consist of clumpy structures rather than spatially smooth distribution because observed molecular gas properties are better explained by the former clumpy model (Solomon et al. 1979, 1987). Each clump can be optically thick, but has random motion inside molecular clouds so that emission from clumps at the other side of molecular clouds is not significantly flux-attenuated by foreground molecular gas clumps (Solomon et al. 1987). The physical properties of individual clumps are assumed to be the same throughout a molecular cloud and among different molecular clouds. In this model, profiles of molecular lines with even different line opacity are expected to be similar. Figure 8 shows similar $v = 0$ $J = 3$–2 emission line profiles of HCN, HCO$^+$, and HNC, supporting the above clumpy molecular gas model for IRAS 20551−4250.

Adopting this clumpy molecular gas model, line opacity comes mostly from the individual line-emitting clumps rather than foreground molecular gas. The flux attenuation factor is
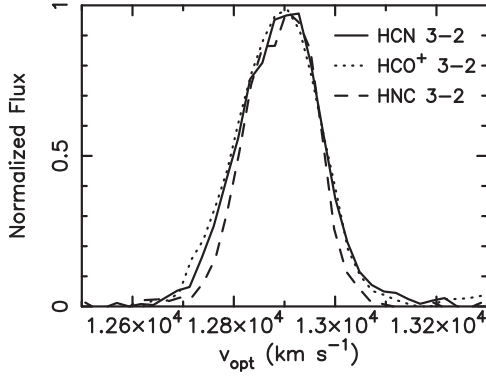
Figure 8. Comparison of the line profile of HCN $J = 3–2$ (solid line), HCO$^+$ $J = 3–2$ (dotted line), and HNC $J = 3–2$ (dashed line; $v = 0$). The abscissa is optical LSR velocity ($v_{opt} \equiv c (\lambda - \lambda_0)/\lambda_0$), and the ordinate is flux normalized by the peak value of the Gaussian fits (Table 3, column 8).

expressed by

$$\text{Flux} - \text{attenuation} = \frac{\tau}{1 - e^{-\tau}}, \qquad (15)$$

where τ is an optical depth, which is proportional to column density. The flux attenuation of 6 for HCN $v = 0$ $J = 3–2$ emission corresponds to $\tau = 6$. In the same way, we obtain $\tau < 2.8$ for HCO$^+$ $v = 0$ $J = 3–2$ emission. For HNC $J = 3–2$, the flux attenuation is estimated to be not substantially larger than unity. We adopt $\tau < 1$ for HNC $v = 0$ $J = 3–2$ emission, in which case the flux attenuation is <1.6. Consequently, we obtain the following optical depth ratio among HCN, HCO$^+$, and HNC $J = 3–2$ at $v = 0$,

$$\text{HCN: HCO}^+\text{: HNC}(\tau) = 1: <0.5: <0.2. \qquad (16)$$

If the optical depth in thermally excited gas is small, the $J = 4–3$ to $J = 3–2$ flux ratio can be higher than that of thermally excited optically thick gas. The possibly higher $J = 4–3$ to $J = 3–2$ flux ratio for HNC (1.8 ± 0.2) than HCN (1.6 ± 0.2; Section 4.1) might be related to the small optical depth of HNC.

The optical depth ratio among $v = 0$ $J = 3–2$ emission lines of HCN, HCO$^+$, and HNC can be roughly estimated independently from the abundance ratio in Equation (14). Considering the transitions between $J = 3$ and $J = 2$ ($v = 0$), the optical depth value is expressed as

$$\tau \propto \nu \times N_2 \times B_{J = 2–3,\text{rot}} \times (1 - g_2 n_3/g_3 n_2), \qquad (17)$$

$$\propto \nu^{-2} \times N_2 \times A_{J = 3–2,\text{rot}} \times (1 - g_2 n_3/g_3 n_2), \qquad (18)$$

where N_2 is the column density at $J = 2$ ($v = 0$), n_J is the number density at $J = 2$ or $J = 3$ ($v = 0$), $B_{J=2–3,\text{rot}}$ is the Einstein B coefficient for rotational transition from $J = 2$ to $J = 3$ ($v = 0$), $A_{J=3–2,\text{rot}}$ is the Einstein A coefficient for spontaneous emission for rotational transition from $J = 3$ to $J = 2$ ($v = 0$), ν is frequency, and g_J is the statistical weight that is related to the J-level in the form of $2J+1$ (Rybicki & Lightman 1979). In IRAS 20551$-$4250, since HCN, HCO$^+$, and HNC are found to be almost thermally excited at $J = 3$ and $J = 4$, the $g_2 n_3/g_3 n_2$ term is expressed with $\exp(-E/k_B T_{\text{kin}})$, where E is the energy level of the J-transition of interest, T_{kin} is the kinetic temperature of molecular gas, and k_B is the Boltzmann constant. For HCN, HCO$^+$, and HNC, since energy

Table 7
Summary of the Ratios of Various Parameters for HCN, HCO$^+$, and HNC

Parameters (1)	HCN:HCO$^+$:HNC (2)
Column density at $v_2 = 1f$, $J = 3$	1:<0.20:0.69
Observed $v_2 = 1f$ to $v = 0$ flux ratio at $J = 3–2$	1:<0.25:1.5
B coefficient from $v = 0$ to $v_2 = 1$	1:1.1:11
Infrared flux used for vibrational excitation	1:0.8:2.5
Predicted infrared radiative pumping rate	1:0.9:27
Predicted $v_2 = 1$ to $v = 0$ column density ratio	1: 0.5:9
Derived abundance	1:<0.4:<0.08
Line opacity derived from isotopologue flux	1:<0.5:<0.2
Line opacity derived from abundance	1:<0.7:<0.1

Note. Col. (1): Parameters used for our discussion in Section 4.3. Col. (2): Ratio among HCN, HCO$^+$, and HNC.

levels and frequencies are almost the same for the same rotational J-transitions at $v = 0$, the term $\nu^{-2} \times (1 - g_2 n_3/g_3 n_2)$ is also nearly identical. Adopting the $A_{J = 3–2,\text{rot}}$ values shown in Table 5, we obtain the following optical depth ratio from the derived abundance ratio in Equation (14),

$$\text{HCN: HCO}^+\text{: HNC}(\tau_2) = 1: <0.7: <0.1. \qquad (19)$$

The two independently derived optical depth ratios in Equations (16) and (19) show consistent results. The ratios of various parameters among HCN, HCO$^+$, and HNC used for our discussion are summarized in Table 7.

We now correct for the flux attenuation by line opacity to derive the intrinsic HCN-to-HCO$^+$ and HCN-to-HNC flux ratios from the observed ratios in Figure 6. For $J = 3–2$, we adopt the flux attenuation with factors of 6, <3, and ~1 for HCN, HCO$^+$, and HNC, respectively (Section 4.3.2, second paragraph). For $J = 4–3$, the observed HCN-to-HCO$^+$ and HCN-to-HNC flux ratios are almost identical to those at $J = 3–2$. Since excitation condition does not significantly change the flux ratios between $J = 3–2$ and $J = 4–3$ in IRAS 20551$-$4250 (Section 4.1) and since the abundance effect should be the same between $J = 3–2$ and $J = 4–3$, the observed flux ratios at $J = 4–3$ can be naturally interpreted with the similar intrinsic flux ratios and flux attenuation to $J = 3–2$. We thus apply the same flux attenuation correction for $J = 4–3$ as employed above for $J = 3–2$.

The intrinsic molecular line flux ratio of IRAS 20551$-$4250 at $J = 3–2$ and $J = 4–3$, after the correction for flux attenuation by line opacity, are plotted as open symbols in Figure 6, which are further deviating from the distribution of starburst-dominated regions. Other data points could also move if opacity-corrected intrinsic flux ratios are used. If HCN flux enhancement is indeed a good signature of AGNs, and if this is due in part to HCN abundance enhancement, then the line opacity of HCN emission and thereby the opacity correction factor of HCN flux relative to HCO$^+$ and HNC could be higher in AGNs than in starburst galaxies. This will move AGNs to the right and upper direction, even deviating from the distribution of starburst galaxies. This could make the HCN-flux-based separation between AGNs and starbursts more solid. Furthermore, if higher HCN opacity is the case in AGNs, while some AGNs show enhanced observed HCN fluxes, other AGNs may not. This could explain the result that some fraction of AGNs do not necessarily show observed HCN flux enhancements (Privon et al. 2015), although it is possible that

the result is partly due to the dilution of the signatures of AGN-affected molecular gas emission by the large contamination from spatially extended starburst-affected molecular gas emission in their large-aperture, single-dish telescope data. Correction for flux attenuation through isotopologue observations (e.g., $H^{13}CN$, $H^{13}CO^+$, $HN^{13}C$, $HC^{15}N$, $H^{15}NC$) is necessary not only for IRAS 20551−4250, but also for other galaxies, to derive intrinsic flux ratios in Figure 6.

Finally, in Figure 6, IRAS 22491−1808 shows no clear infrared-identified buried AGN signatures, and yet shows a high HCN-to-HCO$^+$ flux ratio at $J = 4–3$ (Imanishi & Nakanishi 2013b). For IRAS 22491−1808, the HCN $v_2 = 1f$ $J = 3–2$ emission line has been detected in our ALMA Cycle 2 data (Imanishi 2016) suggesting the presence of a strongly $14\,\mu$m emitting energy source, which is naturally explained by a luminous buried AGN due to AGN-heated hot dust (Sections 1 and 4.3.1). IRAS 22491−1808 may contain an extremely deeply buried AGN whose signatures are not detectable in infrared energy diagnostic methods, but can be detected in (sub)millimeter observations for the first time due to reduced effects of dust extinction. The presence of similar sources, infrared-classified-starbursts with elevated HCN-to-HCO$^+$ flux ratios, is found also at $J = 1–0$ (Costagliola et al. 2011; Privon et al. 2015). ALMA (sub)millimeter observations of these sources are interesting to scrutinize the presence of infrared-elusive, but (sub)millimeter-detectable, extremely deeply buried AGNs.

4.4. Possible Caveats

We here comment a few caveats for our discussion above. First, transitions among rotational J-levels within $v = 0$ and $v_2 = 1$ are not treated in our calculations (Equations (10)–(12)) because the number of currently available molecular J-transition data is not large enough to do this in a reliable manner. This could be the largest uncertainty. However, the similar excitation up to $J = 4$ at $v = 0$ among HCN, HCO$^+$, and HNC, estimated from their similar observed $J = 4–3$ to $J = 3–2$ flux ratios (Section 4.1), suggests that the effects of this uncertainty for our discussion at $J = 3$ and $J = 4$ are expected to be relatively limited, unless excitation at higher J is considerably different among HCN, HCO$^+$, and HNC. When more J-transition data become available, this point will be tested more.

Second, we assumed that HCN, HCO$^+$, and HNC emission both at $v = 0$ and $v_2 = 1$ come from the same region (Section 4.3.1). This is clearly too simplistic. Even though the dipole moments are comparable among HCN, HCO$^+$, and HNC (Section 4.3.1), their critical densities are not perfectly the same. HCO$^+$ has a lower critical density than HCN and HNC by a factor of ~5 for the same J-transition at $v = 0$ (Meijerink et al. 2007; Greve et al. 2009), so that the spatial extent of collisionally excited HCO$^+$ $v = 0$ $J = 3–2$ emission line can be larger than those of HCN/HNC $v = 0$ $J = 3–2$ emission lines if molecular gas has a gradually decreasing radial density distribution from the very center to the outer region in a galaxy (Bigiel & Blitz 2012) due to the decrease of typical density of individual molecular gas clumps. In fact, it is sometimes seen in a galaxy nuclear scale that HCO$^+$ emission is spatially more extended than HCN emission at the same J-transition (Imanishi et al. 2007b; Saito et al. 2015). This is also the case for IRAS 20551−4250 because HCO$^+$ $v = 0$ $J = 3–2$ emission is estimated to be slightly more extended spatially

than HCN/HNC $v = 0$ $J = 3–2$ emission (Section 3). The size of the continuum-emitting region around a buried AGN is also different at $14\,\mu$m (used for the vibrational excitation to $v_2 = 1$ for HCN), $12\,\mu$m (HCO$^+$), and $21.5\,\mu$m (HNC). These different geometries are shown as schematic diagrams in Figure 9. For the $v_2 = 1f$ $J = 3–2$ emission, in the case of constant radial density distribution of molecular gas, since the number of infrared photons per molecule is larger in the close vicinity of an AGN than the outer part, the $v_2 = 1f$ to $v = 0$ flux ratios of HCN/HCO$^+$/HNC should be higher at the inner part, and the bulk of the $v_2 = 1f$ $J = 3–2$ emission is likely to come from the inner region in Figure 9. The emission-weighted size of the $v_2 = 1f$ $J = 3–2$ line can become smaller than that of the $v = 0$ $J = 3–2$ line for HCN/HCO$^+$/HNC. The difference of the $v_2 = 1f$ to $v = 0$ flux ratios between the inner and outer parts and the emission-weighted size difference between $v_2 = 1f$ and $v = 0$ are reduced if molecular gas has a decreasing radial density distribution from the galaxy center to the outer part. We need to consider how these differences in geometry could alter our results obtained based on the assumption that HCN/HCO$^+$/HNC $v = 0$ and $v_2 = 1f$ lines come from the same volume.

Regarding the size difference between $v_2 = 1f$ $J = 3–2$ and $v = 0$ $J = 3–2$ emission, the total fluxes of HCN/HCO$^+$/HNC $v_2 = 1f$ $J = 3–2$ emission lines from molecular gas in Figure 9 are primarily determined by the number of infrared photons which are absorbed and used for the vibrational excitation to $v_2 = 1$. As long as (a) the covering solid angle around the central infrared continuum-emitting energy source does not differ a lot among HCN, HCO$^+$, and HNC, and (b) the bulk of the $v_2 = 1f$ $J = 3–2$ emission is covered within our ALMA beam, then our discussion in Section 4.3 is essentially unchanged. Both conditions (a) and (b) are likely to be met.

Regarding the size difference of the infrared continuum-emitting regions among HCN/HCO$^+$/HNC, the most important factor for our infrared radiative pumping calculations of $v_2 = 1f$ fluxes in Section 4.3.1 is again the number of infrared photons used for the vibrational excitation to $v_2 = 1$. The slight difference of the spatial extent of continuum-emitting regions at different infrared wavelengths will not alter our results significantly, as long as (a) the infrared continuum-emitting regions are more compact than the surrounding molecular gas, and (b) the covering fraction around the central energy source is similar among HCN, HCO$^+$, and HNC. Both conditions (a) and (b) are expected to be fulfilled.

Regarding the size difference of $v = 0$ $J = 3–2$ emission among HCN, HCO$^+$, and HNC, the HCO$^+$ $J = 3–2$ emission is estimated to be spatially more extended than the HCN/HNC $J = 3–2$ emission inside the ALMA beam (Section 3). In this case, the source solid angle (Ω) in Equation (1) becomes larger for HCO$^+$ $J = 3–2$ than HCN/HNC $J = 3–2$, and the HCO$^+$ $J = 3–2$ ($v = 0$) column density is smaller than our estimate. This affects our discussion of column density and thereby abundance. In fact, if both HCN $J = 3–2$ and HCO$^+$ $J = 3–2$ emission are thermalized (excitation temperature is comparable to the kinetic temperature of molecular gas; Section 4.1) and if the optical depth of HCN $J = 3–2$ line is larger than that of HCO$^+$ $J = 3–2$ line (Section 4.3.2), then the HCO$^+$ $J = 3–2$ flux cannot be larger than the HCN $J = 3–2$ flux, as long as both lines are emitted from the same volume because their frequencies are almost identical. The HCO$^+$ $v = 0$ $J = 3–2$ to HCN $v = 0$ $J = 3–2$ flux ratio of 1.4 (Table 5) can
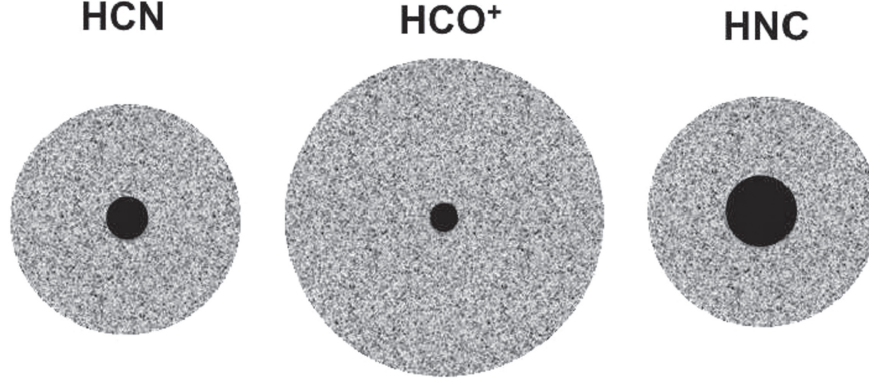
HCN　　　　HCO$^+$　　　　HNC

Figure 9. Schematic diagram of the spatial distribution of nuclear molecular gas and continuum-emitting regions for infrared radiative pumping for HCN, HCO$^+$, and HNC. The large gray circles are the expected sizes of the HCN $J = 3$–2, HCO$^+$ $J = 3$–2, and HNC $J = 3$–2 ($v = 0$) line-emitting regions, assuming gradually decreasing radial density distribution of molecular gas from the very center to the outer region in a galaxy (Bigiel & Blitz 2012). The size is expected to be larger for HCO$^+$ than HCN and HNC, due to a factor of $\sim$5 lower critical density for HCO$^+$ than HCN and HNC (see Section 4.4). It is likely that these regions consist of individual molecular gas clumps (see Section 4.3.2), and that HCO$^+$ is less clumpy (occupies a larger volume fraction) than HCN and HNC due to the lower HCO$^+$ critical density (see Section 4.4). The central filled black circles represent the infrared 14 μm (HCN), 12 μm (HCO$^+$), 21.5 μm (HNC) continuum-emitting regions. The size of the infrared continuum-emitting region is expected to be the smallest for HCO$^+$ and the largest for HNC. The bulk of the HCN/HCO$^+$/HNC $v_2 = 1$f $J = 3$–2 emission is likely to come from the inner region of the gray circle, where infrared radiation density from the central energy source is high (Section 4.4).

be explained if the HCO$^+$ $v = 0$ $J = 3$–2 line-emitting region is >1.4 times larger in Ω than the HCN $J = 3$–2 line-emitting region within our ALMA beam. In our ALMA data, the spatial extent of HCO$^+$ $v = 0$ $J = 3$–2 emission is estimated to be larger than those of HCN/HNC $v = 0$ $J = 3$–2 emission by a factor of $\sim$1.5 in Ω (Section 3). In this case, the actual HCO$^+$ column density (abundance) relative to HCN will decrease by $\sim$50%. This will even strengthen our result that HCN-to-HCO$^+$ abundance ratio is high in the IRAS 20551$-$4250 nucleus. It is also possible that due to the lower critical density of HCO$^+$ $v = 0$ $J = 3$–2 than HCN/HNC $v = 0$ $J = 3$–2, the size of individual molecular gas clumps is larger for HCO$^+$ $v = 0$ $J = 3$–2 than HCN/HNC $v = 0$ $J = 3$–2 if each molecular clump has a decreasing radial density distribution (Gierens et al. 1992; Imanishi et al. 2007b). In this case, HCO$^+$ $v = 0$ $J = 3$–2 emission could occupy a larger volume fraction inside a molecular cloud than the HCN/HNC $v = 0$ $J = 3$–2 emission. This will also work to decrease the HCO$^+$ column density (abundance) relative to HCN and HNC, which again reinforces our main result of enhanced HCN-to-HCO$^+$ abundance ratio in the nucleus of IRAS 20551$-$4250.

Third, we assumed that the observed mid-infrared continuum is dominated by AGN-heated hot dust emission (Section 4.3.1). Even though this is the case for IRAS 20551$-$4250, there may be non-negligible contribution from starburst emission to the observed mid-infrared flux. Since starburst-heated dust usually has cooler temperature than AGN-heated dust, the starburst contribution to the observed mid-infrared flux becomes relatively higher at a longer wavelength (Farrah et al. 2002, 2003; Prouton et al. 2004; Vega et al. 2008; Ruiz et al. 2010). The relative contribution from starbursts can be larger at 21.5 μm (for HNC) than 12 μm (HCO$^+$) and 14 μm (HCN). If a certain fraction of infrared 21.5 μm flux comes from starbursts rather than the buried AGN, the AGN-origin HNC term in Equation (13) will decrease. Even if this slightly modifies the HNC term in Equation (13), our main result of very high HCN-to-HNC abundance ratio (Section 4.3.1) will not change.

Summarizing, even though neglecting the transitions among rotational J-levels within $v = 0$ and $v_2 = 1$ needs to be tested in future data, our main result is robust to possible ambiguity of

the assumed geometry of HCN, HCO$^+$, and HNC emission regions around energy sources.

4.5. Role of Infrared Radiative Pumping

The excitation temperature (T_{ex}) is related to the column density at level u (N_u) in the form of

$$N_u = \frac{N_{mol}}{Q(T)} g_u \exp\left(-\frac{E_u}{k_B T_{ex}}\right), \qquad (20)$$

where N_{mol} is the total column density of a given molecule, Q (T) is a partition function, E_u is an energy at level u above the ground state, k_B is the Boltzmann constant, and g_u is the statistical weight. The excitation temperatures (T_{ex}) in IRAS 20551$-$4250, based on the observed fluxes in this paper and Imanishi & Nakanishi (2013b) are shown in Table 8. If $v_2 = 1$ emission is optically thin and $v = 0$ emission is optically thick, the intrinsic vibrational excitation temperature (T_{ex-vib}) after correcting for line opacity will be smaller than that based on the observed flux ratio between $v_2 = 1$ and $v = 0$. For HCN, the T_{ex-vib} values corrected for the flux attenuation with a factor of 6 for HCN $v = 0$ $J = 3$–2 emission (Section 4.3.2) are also shown in Table 8. The same opacity correction is applied for HCN $v = 0$ $J = 4$–3 emission (see Section 4.3.2).

In Table 6, we also show the HCN $v_2 = 1$f to $v = 0$ flux ratios at $J = 4$–3 and/or $J = 3$–2 in NGC 4418 and Mrk 231, for which flux attenuation of $v = 0$ emission is quantitatively estimated (Sakamoto et al. 2010; Aalto et al. 2015b). The observed ratios are similar between IRAS 20551$-$4250 and Mrk 231. For NGC 4418, the observed HCN $v_2 = 1$f to $v = 0$ flux ratios at $J = 3$–2 and $J = 4$–3 are higher by a factor of 4–5 than IRAS 20551$-$4250 and Mrk 231. However, Sakamoto et al. (2010) estimated a factor of $\sim$20 flux attenuation of HCN $v = 0$ $J = 4$–3 emission in NGC 4418. If we apply this correction, the intrinsic HCN $v_2 = 1$f to $v = 0$ flux ratios for NGC 4418 become $\sim$0.01 at $J = 3$–2 and $J = 4$–3. For HCN emission from IRAS 20551$-$4250, assuming flux attenuation by a factor of 6 (see Section 4.3.2), the intrinsic HCN $v_2 = 1$f to $v = 0$ flux ratios at $J = 3$–2 and $J = 4$–3 become $\sim$0.01. For

Table 8
Excitation Temperature for IRAS 20551−4250

Molecule (1)	$(v_2, J; v, J)$ (2)	T_{ex} (K) (3)
HCN	(1f, 3; 0, 3)	340 (210)
	(1f, 4; 0, 4)	330 (210)
	(1f, 3; 0, 4)	430 (245)
	(1f, 4; 0, 3)	275 (185)
	(1f, 4; 1f, 3)	23
	(0, 4; 0, 3)	25
HNC	(1f, 3; 0, 3)	250
HCO⁺	(1f, 3; 0, 3)	<270

Note. Col. (1): Molecular line. Col. (2): Transition. Col. (3): Excitation temperature (T_{ex}) in (K). For the HCN $v = 0$ $J = 3$–2 and $J = 4$–3 emission, flux attenuation with a factor of 6 is estimated (Section 4.3.2). In first four rows, T_{ex} values, after the correction by a factor of 6, are shown in the parentheses.

Mrk 231, if we adopt a factor of ~10 flux attenuation of HCN $v = 0$ $J = 3$–2 emission (Aalto et al. 2015b), the intrinsic HCN $v_2 = 1f$ to $v = 0$ flux ratio at $J = 3$–2 becomes ~0.005. Given the almost identical Einstein A coefficient at $v_2 = 1f$ and $v = 0$ for the same J-transition lines (Table 5), we can derive that the population ($\propto$ flux/A) at $v_2 = 1$ ($J = 3,4$) is approximately 0.5–1% of that at $v = 0$ ($J = 3,4$) in IRAS 20551−4250, NGC 4418, and Mrk 231. The observed HCN $v_2 = 1f$ to $v = 0$ flux ratios at $J = 4$–3 or $J = 3$–2 shown by Aalto et al. (2015a) range from ~0.1 (Zw 049.057 and IRAS 17208−0014) to ~0.2 (IC 860 and Arp 220W). The information of flux attenuation for $v = 0$ emission is needed to derive the intrinsic ratio. These four sources are not included in our quantitative discussion about intrinsic flux ratios, but it is quite possible that these sources have similarly low intrinsic values to the above three LIRGs because large line opacities for the $v = 0$ emission are argued (Aalto et al. 2015a; Martin et al. 2016).

Although the HCN population at $v_2 = 1$ is only ~1% of that at $v = 0$ for the same J-level, the Einstein A coefficient from $v_2 = 1f$ $J = 4$ to $v = 0$ $J = 3$ (1.7–3.7 s^{-1}; Deguchi et al. 1986; Ziurys & Turner 1986; Aalto et al. 2007) is nearly three orders of magnitude larger than that from $v = 0$ $J = 4$ to $v = 0$ $J = 3$ (0.002 s^{-1}; Table 5). The photon number of the transition from $v_2 = 1f$ $J = 4$ to $v = 0$ $J = 3$ is estimated to be an order of magnitude higher than that from $v = 0$ $J = 4$ to $v = 0$ $J = 3$. Therefore, we can conclude that infrared radiative pumping affects rotational excitation at $v = 0$, and thus could alter the $v = 0$ J-transition flux ratios compared to collisional excitation alone as the excitation mechanism.

The condition where infrared radiative pumping can have a significant influence on the HCN rotational excitation at $v = 0$ is defined as

$$T_{ex-vib} > \frac{T_0}{\ln \frac{A_{v2=1-0,vib}}{A_{rot}}}, \quad (21)$$

where T_{ex-vib} is the $v_2 = 1$ vibrational excitation temperature, T_0 is the energy level of HCN $v_2 = 1f$ $J = 4$ or $J = 3$, $A_{v2=1-0,vib}$ is the Einstein A coefficient from $v_2 = 1$ to $v = 0$, and A_{rot} is the Einstein A coefficient between J-levels at $v = 0$ (Carrol & Goldsmith 1981; Sakamoto et al. 2010; Mills et al. 2013). For $J = 3$–2, adopting $T_0 = 1050.0$ (K; Table 5), $A_{v2=1-0,}$

$_{vib} = 1.7$ s^{-1} (Section 4.3.1), and $A_{3-2,rot} = 8.4 \times 10^{-4}$ (Table 5), the right-hand column becomes ~140 (K). For $J = 4$–3, adopting $T_0 = 1067.1$ (K; Table 5), $A_{v2=1-0,vib} = 1.7$ s^{-1} (Section 4.3.1), and $A_{4-3,rot} = 20.6 \times 10^{-4}$ (Table 5), the right-hand column becomes ~160 (K). The T_{ex-vib} in the left-hand column is >275 (K), if we neglect line opacity for HCN $v = 0$ emission (Table 8). Even if flux attenuation by a factor of 6 for HCN $v = 0$ emission is included, the T_{ex-vib} value is still >185 (K; Table 8). Thus, the condition in Equation (21) is fulfilled for HCN at $J = 4$ and 3 in IRAS 20551−4250.

For HNC $J = 3$–2, the same logic is applicable. The value in the right-hand column is 80 (K) for HNC $J = 3$–2. However, the T_{ex-vib} value in the left-hand column is 250 (K), where the observed $v_2 = 1f$ and $v = 0$ fluxes are used, because the flux attenuation of HNC $v = 0$ $J = 3$–2 emission is not estimated to be significantly larger than unity (Section 4.3.2). We can therefore conclude that infrared radiative pumping affects the HNC rotational excitation at $v = 0$ as well.

For HCO⁺ $J = 3$–2, the values in the left-hand and right-hand columns are <270 (K) and 160 (K), respectively, where the observed $v_2 = 1f$ and $v = 0$ fluxes are used because the estimated flux attenuation for HCO⁺ $v = 0$ $J = 3$–2 emission is <3 (Section 4.3.2). Although the HCO⁺ $v_2 = 1f$ $J = 3$–2 flux is an upper limit, if the actual flux is larger than 5% of the upper limit, the left-hand column will be higher than the right-hand column, and thus it is still possible that infrared radiative pumping plays some role for HCO⁺.

If infrared radiative pumping is at work to excite HCN/HCO⁺/HNC molecules to the $v_2 = 1$ level, a sufficient number of infrared photons have to be absorbed. Figure 10 displays the *Spitzer* IRS high-resolution ($R \sim 600$) spectra of IRAS 20551 −4250 at $\lambda_{rest} \sim 14\,\mu m$ (corresponding to HCN $v_2 = 1$ absorption), 12 μm (HCO⁺), and 21.5 μm (HNC; Lebouteiller et al. 2015). Although possible signatures relating to the HCN $v_2 = 1$ absorption features may be present, the absorption features are not clear at the expected wavelengths of HCO⁺ and HNC $v_2 = 1$ absorption. Assuming that HCN/HCO⁺/HNC $v_2 = 1$ absorption features in the infrared spectra have the same velocity profile as the HCN/HCO⁺/HNC $v_2 = 1f$ $J = 3$–2 emission features at 1 mm (~270 GHz), the required condition for infrared radiative pumping to work is

$$\sum_{i=P,Q,R} f_i S_{IR}/\lambda_{IR} > S_{rot}/\lambda_{rot} \quad (22)$$

(Sakamoto et al. 2010). Here, S_{IR} is the continuum flux density (in (Jy)) around the absorption wavelength λ_{IR}, f_i is the fractional absorption depth at the absorption peak, and S_{rot} is the peak flux density (in (Jy)) of the $v_2 = 1f$ J-transition line emission at the wavelength λ_{rot}. The "$1/\lambda$" term is included, because a unit frequency width for the given same velocity width, $\Delta\nu$, is inversely proportional to λ (= proportional to ν). In the left-hand term, infrared absorption by the P, Q, and R branches is summed. For HCN absorption at $\lambda_{rest} \sim 14.0\,\mu m$, the absorption dip, $f_i S_{IR}$, is at most <0.03 (Jy) in the infrared spectrum (Figure 10). The peak flux of the HCN $v_2 = 1f$ $J = 3$–2 emission line in the millimeter wavelength is ~1.5 (mJy; Figure 4). The upper limit in the left-hand term of Equation (22) is approximately three orders of magnitude larger than the right-hand term. For HCO⁺ and HNC, the dips of infrared absorption features, $f_i S_{IR}$, are at most <0.01 (Jy) and
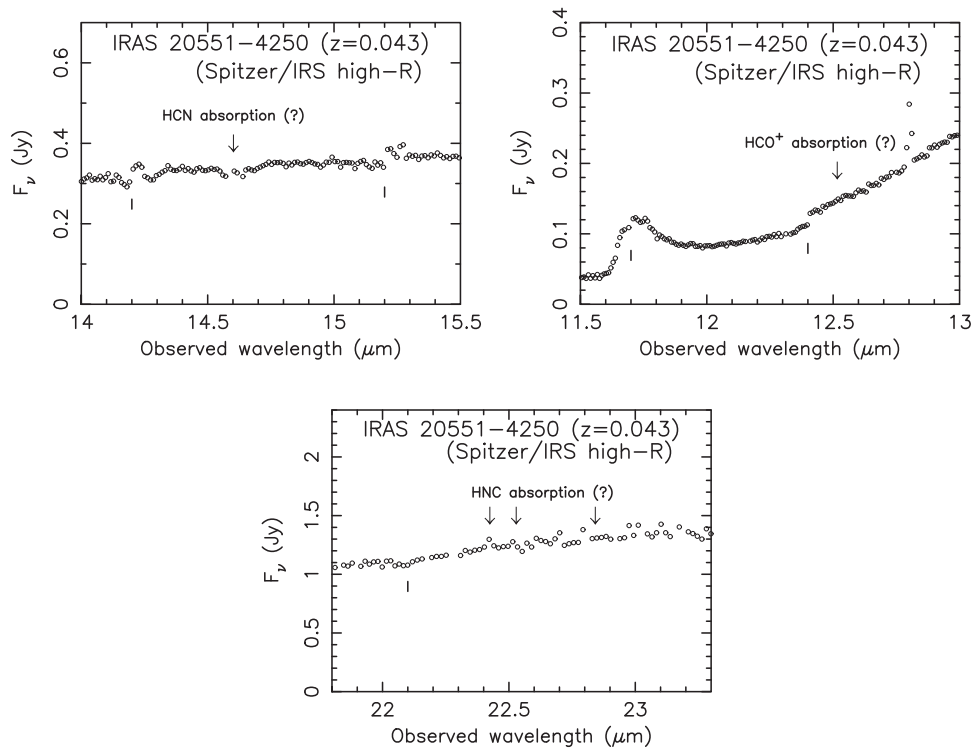
Figure 10. *Spitzer* IRS high-resolution ($R \sim 600$) infrared spectra of IRAS 20551−4250 taken from the Cornell Atlas of *Spitzer*/IRS Sources (CASSIS; Lebouteiller et al. 2015). Zoom-in spectra around HCN, HCO$^+$, and HNC absorption features at $\lambda_{rest} \sim 14$ μm, 12 μm, and 21.5 μm, respectively, are shown. For HCN and HCO$^+$, down arrows are shown at $\lambda_{rest} = 14.0$ μm and 12.0 μm, respectively. For HNC, we plot down arrows at $\lambda_{rest} = 21.5$ μm, 21.6 μm, and 21.9 μm, which correspond to $v_2 = 1$ transition at low J-evels for R, Q, and P branches, respectively (Burkholder et al. 1987). Several small gaps seen in the spectra are due to observations with different spectral settings. These wavelengths at the edge of each spectral setting are indicated as the vertical solid straight lines.

<0.1 (Jy), respectively (Figure 10). The peak fluxes of the HCO$^+$ $v_2 = 1f$ $J = 3–2$ and HNC $v_2 = 1f$ $J = 3–2$ emission lines in the millimeter wavelength are <1.0 (mJy) and ∼0.8 (mJy), respectively (Figure 4). The upper limit and value in the left-hand term of Equation (22) is also about three orders of magnitude larger than the right-hand term for HCO$^+$ and HNC, respectively. Although the energy absorbed by the infrared photons is used for other J-transition lines at $v_2 = 1f$ for HCN/HCO$^+$/HNC, there is a large enough margin for infrared radiative pumping as the source of vibrational excitation of HCN/HCO$^+$/HNC unless the actual strengths of the infrared $v_2 = 1$ absorption features of HCN/HCO$^+$/HNC are more than three orders of magnitude smaller than the current upper limits. The observed velocity widths of HCN and HNC $v_2 = 1f$ $J = 3–2$ emission lines are ∼200 km s^{-1} in FWHM (Table 3). To detect absorption features with this level of velocity width, a spectral resolution with $R > 1500$ is necessary. The minimum required infrared absorption features of HCN/HCO$^+$/HNC are too weak to be detected with the current quality *Spitzer* IRS $R \sim 600$ spectrum. A higher signal-to-noise ratio and spectral resolution spectrum is therefore required to unambiguously detect the infrared $v_2 = 1$ absorption features of HCN/HCO$^+$/HNC, and to better constrain the energetics between absorbed infrared photons and $v_2 = 1f$ J-transition emission lines more quantitatively.

In summary, it is very likely that infrared radiative pumping is at work in IRAS 20551−4250, and therefore the infrared radiative pumping effect must be properly taken into account for HCN and HNC, and possibly for HCO$^+$, too, if we are to

understand rotational excitation at $v = 0$ and J-transition flux ratio at $v = 0$ in IRAS 20551−4250. However, based on the currently available data, it is not yet quantitatively clear what percentages of the observed molecular line fluxes at $v = 0$ are altered by the infrared radiative pumping compared to collisional excitation. Molecular gas rotational J-level populations and fluxes of rotational J-transitions at $v = 0$ in IRAS 20551−4250 are determined by (a) collisional excitation, which is dependent on molecular gas physical parameters (density, kinetic temperature, etc.), and (b) contribution from infrared radiative pumping. Obtaining further molecular line data at other J-transition lines at both $v = 0$ and $v_2 = 1$ will help to better disentangle these two factors and to better understand the physical origin of the observed HCN/HCO$^+$/HNC molecular line flux ratios in IRAS 20551−4250.

5. SUMMARY

We conducted ALMA Cycle 2 observations of the AGN-hosting ULIRG IRAS 20551−4250 at HCN/HCO$^+$/HNC $J = 3–2$ (rotational transition) at both vibrational ground ($v = 0$) and vibrationally excited ($v_2 = 1$) levels. Since our ALMA Cycle 0 observations showed a tentatively detectable (∼5σ) vibrationally excited HCN $v_2 = 1f$ $J = 4–3$ emission line from this source, our new data are useful for investigating (a) whether the vibrationally excited ($v_2 = 1f$) HCN emission line is visible at $J = 3–2$ as well, and (b) the strength of the vibrationally excited ($v_2 = 1f$) $J = 3–2$ emission lines for HCO$^+$ and HNC. The main results of these observations are as follows.

1. HCN, HCO$^+$, and HNC $J = 3$–2 emission lines at the vibrational ground level were clearly detected at the continuum peak position.

2. We detected HCN $v_2 = 1f$ $J = 3$–2 and HNC $v_2 = 1f$ $J = 3$–2 emission lines, based on Gaussian fits of the spectra and integrated intensity (moment 0) maps, supporting the scenario that IRAS 20551−4250 shows detectable vibrationally excited $v_2 = 1f$ J-transition emission lines for both HCN and HNC.

3. The vibrationally excited HCO$^+$ $v_2 = 1f$ $J = 3$–2 emission line was not clearly detected, but a stringent upper limit was in place. The observed $v_2 = 1f$ $J = 3$–2 to $v = 0$ $J = 3$–2 flux ratio for HCO$^+$ is more than a factor of four smaller than those for HCN and HNC.

4. Since collisional excitation is very difficult to significantly populate the $v_2 = 1$ level due to its high energy level (>600 K), we calculated how infrared radiative pumping can achieve the vibrational excitation using the available infrared 5–35 μm spectrum. It was estimated that the infrared radiative pumping rate to $v_2 = 1$ of HCN is comparable to HCO$^+$, but is smaller than HNC by more than an order of magnitude. Our observational results about the $v_2 = 1f$ $J = 3$–2 emission line fluxes of HCN, HCO$^+$, and HNC can naturally be explained if the HCN abundance is greater than a factor of few higher than HCO$^+$ and an order of magnitude higher than HNC. Because of the low observed equivalent widths of the PAH emission features at 5–25 μm, it was interpreted that infrared photons used for the vibrational excitation of HCN/HCO$^+$/HNC mostly come from AGN-heated hot dust emission near an AGN. Thus, the properties of molecular gas derived from the $v_2 = 1f$ emission largely reflect those of AGN-affected molecular gas in the close vicinity of an AGN. In fact, HCN abundance enhancement in the close vicinity of AGNs was argued in several previous works.

5. The observed $v_2 = 1f$ $J = 3$–2 to $v = 0$ $J = 3$–2 flux ratios for HCN/HCO$^+$/HNC and the observed HCN $v = 0$ $J = 3$–2 to H^{13}CN $v = 0$ $J = 3$–2 flux ratio suggest that HCN $v = 0$ $J = 3$–2 emission has a significant line opacity and is flux-attenuated by a factor of 6, whereas the flux attenuation of HCO$^+$ $v = 0$ $J = 3$–2 and HNC $v = 0$ $J = 3$–2 emission lines was estimated to be <3 and ~1, respectively. The higher flux attenuation by line opacity for HCN than HCO$^+$ and HNC is as expected from the estimated higher HCN abundance than HCO$^+$ and HNC.

6. The observed flux ratio and excitation temperature between $v_2 = 1f$ and $v = 0$ suggest that infrared radiative pumping has an effect on rotational excitation at $v = 0$ for HCN and HNC.

7. The HCN-to-HCO$^+$ $J = 3$–2 flux ratio at $v = 0$ is similar to the previously obtained HCN-to-HCO$^+$ $J = 4$–3 flux ratio at $v = 0$ in IRAS 20551−4250, and both are higher than starburst-dominated regions. The enhanced HCN-to-HCO$^+$ flux ratio in this AGN-hosting ULIRG was interpreted to have originated mainly in the enhanced HCN-to-HCO$^+$ abundance ratio and sufficient HCN excitation rather than the substantially higher infrared radiative pumping efficiency of HCN than that of HCO$^+$. When the estimated line opacity for HCN/HCO$^+$/HNC $v = 0$ emission is corrected, the HCN-to-HCO$^+$ $J = 3$–2 and HCN-to-HNC $J = 3$–2 flux ratio at $v = 0$ for IRAS 20551−4250 will increase, even deviating from the ratios found in starburst-dominated regions. If larger HCN line opacity due to enhanced HCN abundance is common in AGNs, AGNs and starburst galaxies will be separated even more in the plot of line-opacity-corrected, intrinsic HCN-to-HCO$^+$ and HCN-to-HNC flux ratios, than in the plot of observed flux ratios. Line opacity correction of other sources is also necessary to refine these molecular line flux ratios for use as an even more solid energy diagnostic method of dust/gas-rich ULIRGs.

8. Various emission lines, other than the targeted HCN/HCO$^+$/HNC, were also detected, including HOC$^+$, SO$_2$, SO, H^{13}CN, HC$_3$N, and CH$_3$CCH, demonstrating the high sensitivity of ALMA and the abundant presence of excited molecular gas by the nuclear energy source in IRAS 20551−4250.

REFERENCES

Aalto, S., Booth, R. S., Black, J. H., & Johansson, L. E. B. 1995, A&A, 300, 369

Aalto, S., Costagliola, S., Martin, F., et al. 2015a, A&A, 584, 42

Aalto, S., Garcia-Burillo, S., Muller, S., et al. 2015b, A&A, 574, A85

Aalto, S., Spaans, M., Wiedner, M. C., & Huttemeister, S. 2007, A&A, 464, 193

Amano, T. 1983, JChPh, 79, 7

Antonucci, R. R. J., & Millar, J. S. 1985, ApJ, 297, 621

Apponi, A. J., Pesch, T. C., & Ziurys, L. M. 1999, ApJL, 519, L89

Apponi, A. J., & Ziurys, L. M. 1997, ApJ, 481, 800

Baan, W. A., Henkel, C., Loenen, A. F., Baudry, A., & Wiklind, T. 2008, A&A, 477, 747

Bardeen, J. M. 1970, Natur, 226, 64

Bigiel, F., & Blitz, L. 2012, ApJ, 756, 183

Blake, G. A., Sutton, E. C., Masson, C. R., & Phillips, T. G. 1986, ApJS, 60, 357

Burkholder, J. B., Sinha, A., Hammer, P. D., & Howard, C. J. 1987, JMoSp, 126, 72

Carrol, T. J., & Goldsmith, P. F. 1981, ApJ, 245, 891

Costagliola, F., & Aalto, S. 2010, A&A, 515, A71

Costagliola, F., Aalto, S., Rodriguez, M. I., et al. 2011, A&A, 528, A30

Costagliola, F., Aalto, S., Sakamoto, K., et al. 2013, A&A, 556, 66

Costagliola, F., Sakamoto, K., Muller, S., et al. 2015, A&A, 582, A91

Davies, P. B., Hamilton, P. A., & Rothwell, W. J. 1984, JChPh, 81, 1598

Debuhr, J., Quataert, E., & Ma, C-P. 2011, MNRAS, 412, 1341

Deguchi, S., Claussen, M. J., & Goldsmith, P. F. 1986, ApJ, 303, 810

Duc, P.-A., Mirabel, I. F., & Maza, J. 1997, A&AS, 124, 533

Evans, A. S., Becklin, E. E., Scoville, N. Z., et al. 2003, AJ, 125, 2341
Farrah, D., Afonso, J., Efstathiou, A., et al. 2003, MNRAS, 343, 585
Farrah, D., Serjeant, S., Efstathiou, A., Rowan-Robinson, M., & Verma, A. 2002, MNRAS, 336, 1163
Ferrarese, L., & Merritt, D. 2000, ApJL, 539, L9
Foster, S. C., & McKellar, A. R. W. 1984, JChPh, 81, 3424
Foster, S. C., McKellar, A. R. W., & Sears, T. J. 1984, JChPh, 81, 1
Franceschini, A., Braito, V., Persic, M., et al. 2003, MNRAS, 343, 1181
Fritz, T. K., Gillessen, S., Dodds-Eden, K., et al. 2011, ApJ, 737, 73
Garcia-Burillo, S., Combes, F., Usero, A., et al. 2014, A&A, 567, 125
Garcia-Burillo, S., Gracia-Carpio, J., Guelin, M., et al. 2006, ApJL, 645, L17
Genzel, R., Lutz, D., Sturm, E., et al. 1998, ApJ, 498, 579
Gierens, K. M., Stutzki, J., & Winnewisser, G. 1992, A&A, 259, 271
Godard, B., Falgarone, E., Gerin, M., Hily-Blant, P., & De Luca, M. 2010, A&A, 520, A20
Goldsmith, P. F., & Langer, W. D. 1999, ApJ, 517, 209
Gracia-Carpio, J., Garcia-Burillo, S., Planesas, P., & Colina, L. 2006, ApJL, 640, L135
Graninger, D. M., Herbst, E., Öberg, K. I., & Vasyunin, A. I. 2014, ApJ, 787, 74
Greaves, J. S., & White, G. J. 1991, A&AS, 91, 237
Greve, T. R., Papadopoulos, P. P., Gao, Y., & Radford, S. J. E. 2009, ApJ, 692, 1432
Gultekin, K., Richstone, D. O., Gebhardt, K., et al. 2009, ApJ, 698, 198
Harada, N., Herbst, E., & Wakelam, V. 2010, ApJ, 721, 1570
Harada, N., Thompson, T. A., & Herbst, E. 2013, ApJ, 765, 108
Henkel, C., Asiri, H., Ao, Y., et al. 2014, A&A, 565, A3
Henkel, C., & Mauersberger, R. 1993, A&A, 274, 730
Henkel, C., Mauersberger, R., Wiklind, T., et al. 1993, A&A, 268, L17
Hirota, T., Yamamoto, S., Mikami, H., & Ohishi, M. 1998, ApJ, 503, 717
Hopkins, P. F., Hernquist, L., Cox, T. J., et al. 2005, ApJ, 630, 705
Hopkins, P. F., Hernquist, L., Cox, T. J., et al. 2006, ApJS, 163, 1
Hopkins, P. F., Hernquist, L., Cox, T. J., & Keres, D. 2008, ApJS, 175, 356
Imanishi, M. 2009, ApJ, 694, 751
Imanishi, M., & Dudley, C. C. 2000, ApJ, 545, 701
Imanishi, M., Dudley, C. C., Maiolino, R., et al. 2007a, ApJS, 171, 72
Imanishi, M., Imase, K., Oi, N., & Ichikawa, K. 2011, AJ, 141, 156
Imanishi, M., Maiolino, R., & Nakagawa, T. 2010a, ApJ, 709, 801
Imanishi, M., Nakagawa, T., Shirahata, M., Ohyama, Y., & Onaka, T. 2010b, ApJ, 721, 1233
Imanishi, M., & Nakanishi, K. 2006, PASJ, 58, 813
Imanishi, M., & Nakanishi, K. 2013a, AJ, 146, 47
Imanishi, M., & Nakanishi, K. 2013b, AJ, 146, 91
Imanishi, M., & Nakanishi, K. 2014, AJ, 148, 9
Imanishi, M., Nakanishi, K., & Izumi, T. 2016, AJ, submitted
Imanishi, M., Nakanishi, K., & Kohno, K. 2006, AJ, 131, 2888
Imanishi, M., Nakanishi, K., Kuno, N., & Kohno, K. 2004, AJ, 128, 2037
Imanishi, M., Nakanishi, K., Tamura, Y., Oi, N., & Kohno, K. 2007b, AJ, 134, 2366
Imanishi, M., Nakanishi, K., Tamura, Y., & Peng, C.-H. 2009, AJ, 137, 3581
Iono, D., Saito, T., Yun, M. S., et al. 2013, PASJ, 65, L7
Izumi, T., Kohno, K., Aalto, S., et al. 2015, ApJ, 811, 39
Izumi, T., Kohno, K., Aalto, S., et al. 2016, ApJ, 818, 42
Izumi, T., Kohno, K., Martin, S., et al. 2013, PASJ, 65, 100
Kauffmann, G., Heckman, T. M., Tremonti, C., et al. 2003, MNRAS, 346, 1055
Kawaguchi, K., Yamada, C., Saito, S., & Hirota, E. 1985, JChPh, 82, 1750
Kewley, L. J., Heisler, C. A., Dopita, M. A., & Lumsden, S. 2001, ApJS, 132, 37
Kohno, K. 2005, in AIP Conf. Ser. 783, The Evolution of Starbursts, ed. S. Hüttemeister et al. (Melville, NY: AIP), 203
Komatsu, E., Dunkley, J., Nolta, M. R., et al. 2009, ApJS, 180, 330
Krips, M., Neri, R., Garcia-Burillo, S., et al. 2008, ApJ, 677, 262
Lahuis, F., Spoon, H. W. W., Tielens, A. G. G. M., et al. 2007, ApJ, 659, 296
Lebouteiller, V., Barry, D. J., Goes, C., et al. 2015, ApJS, 218, 21
Lintott, C., & Viti, S. 2006, ApJL, 646, L37
Liu, X.-L., Wang, J-J., & Xu, J-L. 2013, MNRAS, 431, 27
Magorrian, J., Tremaine, S., Richstone, D., et al. 1998, ApJ, 115, 2285

Martin, S., Aalto, S., Sakamoto, K., et al. 2016, A&A, 590, A25
Martin, S., Aladro, R., Martin-Pintado, J., & Mauersberger, R. 2010, A&A, 522, A62
Mauclaire, G., Lemaire, J., Heninger, M., et al. 1995, IJMSI, 149, 487
McConnell, N. J., & Ma, C.-P. 2013, ApJ, 764, 184
Meijerink, R., & Spaans, M. 2005, A&A, 436, 397
Meijerink, R., Spaans, M., & Israel, F. P. 2007, A&A, 461, 793
Mills, E. A. C., Güsten, R., Requena-Torres, M. A., & Morris, M. R. 2013, ApJ, 779, 47
Moorwood, A. F. M. 1986, A&A, 166, 4
Müller, H. S. P., Schlöder, F., Stutzki, J., & Winnewisser, G. 2005, JMoSt, 742, 215
Nagy, Z., van der Tak, F. F. S., Fuller, G. A., & Plume, R. 2015, A&A, 577, A127
Nakanishi, K., Okumura, S. K., Kohno, K., Kawabe, R., & Nakagawa, T. 2005, PASJ, 57, 575
Nardini, E., Risaliti, G., Salvati, M., et al. 2008, MNRAS, 385, L130
Nardini, E., Risaliti, G., Salvati, M., et al. 2009, MNRAS, 399, 1373
Nardini, E., Risaliti, G., Watabe, Y., Salvati, M., & Sani, E. 2010, MNRAS, 405, 2505
Nishiyama, S., Nagata, T., Tamura, M., et al. 2008, ApJ, 680, 1174
Nishiyama, S., Tamura, M., Hatano, H., et al. 2009, ApJ, 696, 1407
Petry, D. & CASA Development Team 2012, in ASP Conf. Ser. 461, Astronomical Data Analysis Software and Systems XXI, ed. P. Ballester, D. Egret, & N. P. F. Lorente (San Francisco, CA: ASP), 849
Privon, G. C., Herrero-Illana, R., Evans, A. S., et al. 2015, ApJ, 814, 39
Prouton, O. R., Bressan, A., Clemens, M., et al. 2004, A&A, 421, 115
Ranalli, P., Comastri, A., & Setti, G. 2003, A&A, 399, 39
Rangwala, N., Maloney, P. R., Glenn, J., et al. 2011, ApJ, 743, 94
Risaliti, G., Maiolino, R., Marconi, A., et al. 2006, MNRAS, 365, 303
Roche, P. F., & Aitken, D. K. 1984, MNRAS, 208, 481
Roche, P. F., & Aitken, D. K. 1985, MNRAS, 215, 425
Rothberg, B., & Joseph, R. D. 2004, AJ, 128, 2098
Ruiz, A., Miniutti, G., Panessa, F., & Carrera, F. J. 2010, A&A, 515, A99
Rybicki, G. B., & Lightman, A. P. 1979, Radiative Processes in Astrophysics (New York, NY: Wiley)
Saito, T., Iono, D., Yun, M. S., et al. 2015, ApJ, 803, 60
Sakamoto, K., Aalto, S., Costagliola, F., et al. 2013, ApJ, 764, 42
Sakamoto, K., Aalto, S., Evans, A. S., Wiedner, M., & Wilner, D. 2010, ApJL, 725, L228
Sanders, D. B., Mazzarella, J. M., Kim, D.-C., Surace, J. A., & Soifer, B. T. 2003, AJ, 126, 1607
Sani, E., Risaliti, G., Salvati, M., et al. 2008, ApJ, 675, 96
Sargsyan, L., Weedman, D., Lebouteiller, V., et al. 2011, ApJ, 730, 19
Savage, C., & Ziurys, L. M. 2004, ApJ, 616, 966
Schilke, P., Walmsley, C. M., & Pineau des Forets, G. 1992, A&A, 256, 595
Shang, Z., Brotherton, M. S., Wills, B. J., et al. 2011, ApJ, 196, 2
Snell, R. L., Narayanan, G., Yun, M. S., et al. 2011, ApJ, 141, 38
Solomon, P. M., Rivolo, A. R., Barrett, J., et al. 1987, ApJ, 319, 730
Solomon, P. M., Scoville, N. Z., & Sanders, D. B. 1979, ApJL, 232, L89
Solomon, P. M., & Vanden Bout, P. A. 2005, ARA&A, 43, 677
Spoon, H. W. W., Keane, J. V., Tielens, A. G. G. M., Lutz, D., & Moorwood, A. F. M. 2001, A&A, 365, L353
Stock, D. J., Peeters, E., Choi, W. D.-Y., & Shannon, M. J. 2014, ApJ, 791, 99
Thorne, K. S. 1974, ApJ, 191, 507
Townes, C. H., & Schawlow, A. L. 1975, Microwave Spectroscopy (New York: Dover Publications)
Ueda, J., Iono, D., Yun, M. S., et al. 2014, ApJS, 214, 1
Veach, T. J., Groppi, C., & Hedded, A. 2013, ApJL, 765, L34
Vega, O., Clemens, M. S., Bressan, A., et al. 2008, A&A, 484, 631
Veilleux, S., Melendez, M., Sturm, E., et al. 2013, ApJ, 776, 27
Veilleux, S., & Osterbrock, D. E. 1987, ApJS, 63, 295
Voit, G. M. 1992, MNRAS, 258, 841
Weiss, A., Downes, D., Neri, R., et al. 2007, A&A, 467, 955
Yamada, M., Wada, K., & Tomisaka, K. 2007, ApJ, 671, 73
Yuan, T.-T., Kewley, L. J., & Sanders, D. B. 2010, ApJ, 709, 884
Ziurys, L. M., & Turner, B. E. 1986, ApJL, 300, L19